# Anaerobic oxidation of methane alters sediment records of sulfur, iron and phosphorus in the Black Sea

Matthias Egger[1], Peter Kraal[1], Tom Jilbert[1,2], Fatimah Sulu-Gambari[1], Célia J. Sapart[3,4], Thomas Röckmann[3] and Caroline P. Slomp[1]

[1]Department of Earth Sciences – Geochemistry, Faculty of Geosciences, Utrecht University, P.O. Box 80021, 3508 TA, Utrecht, The Netherlands
[2]Now at: Department of Environmental Sciences, Faculty of Biological and Environmental Sciences, University of Helsinki, P.O. Box 65 (Viikinkaari 2a), 00014 Helsinki, Finland
[3]Institute for Marine and Atmospheric Research Utrecht (IMAU), Utrecht University, Princetonplein 5, 3584 CC Utrecht, The Netherlands
[4]Laboratoire de Glaciologie, Université Libre de Bruxelles, Belgium

*Correspondence to*: Matthias Egger (m.j.egger@uu.nl)

**Abstract.** The surface sediments in the Black Sea are underlain by extensive deposits of iron (Fe) oxide-rich lake sediments that were deposited prior to the inflow of marine Mediterranean Sea waters ca. 9000 years ago. The subsequent downward diffusion of marine sulfate into the methane-bearing lake sediments has led to a multitude of diagenetic reactions in the sulfate-methane transition zone (SMTZ), including anaerobic oxidation of methane (AOM) with sulfate. While the sedimentary cycles of sulfur (S), methane and Fe in the SMTZ have been extensively studied, relatively little is known about the diagenetic alterations of the sediment record occurring below the SMTZ. Here we combine detailed geochemical analyses of the sediment and pore water with multicomponent diagenetic modeling to study the diagenetic alterations below the SMTZ at two sites in the western Black Sea. We focus on the dynamics of Fe, S and phosphorus (P) and demonstrate that diagenesis has strongly overprinted the sedimentary burial records of these elements. In line with previous studies in the Black Sea, we show that sulfate-mediated AOM substantially enhances the downward diffusive flux of sulfide into the deep limnic deposits. During this downward sulfidization, Fe oxides, Fe carbonates and Fe phosphates (e.g. vivianite) are converted to sulfide phases, leading to an enrichment in solid phase S and the release of phosphate to the pore water. Below the sulfidization front, high concentrations of dissolved ferrous Fe ($Fe^{2+}$) lead to sequestration of downward diffusing phosphate as authigenic vivianite, resulting in a transient accumulation of total P directly below the sulfidization front. Our model results further demonstrate that downward migrating sulfide becomes partly re-oxidized to sulfate due to reactions with oxidized Fe minerals, fueling a cryptic S cycle and thus stimulating slow rates of sulfate-driven AOM ($\sim$ 1 - 100 pmol cm$^{-3}$ d$^{-1}$) in the sulfate-depleted limnic deposits. However, this process is unlikely to explain the observed release of dissolved $Fe^{2+}$ below the SMTZ. Instead, we suggest that besides organoclastic Fe oxide reduction and reactivation of less reactive Fe oxides by methanogens, AOM coupled to the reduction of Fe oxides may also provide a possible mechanism for the high concentrations of $Fe^{2+}$ in the pore water at depth. Our results reveal that methane plays a key role in the diagenetic alterations of Fe, S and P records in Black Sea sediments. The downward sulfidization into the limnic deposits is enhanced through sulfate-driven AOM with sulfate and AOM with Fe oxides may provide a deep source of dissolved $Fe^{2+}$ that drives the sequestration of P in vivianite below the sulfidization front.

## 1      Introduction

Anaerobic oxidation of methane (AOM), a process initially regarded as a biogeochemical curiosity, functions as an important sink for oceanic methane ($CH_4$) by consuming > 90 % of all $CH_4$ produced in marine sediments (Knittel and Boetius, 2009; Reeburgh, 2007). Although recent studies indicate that the biological oxidation of $CH_4$ could be coupled to various additional electron acceptors such as nitrate and nitrite (Ettwig et al., 2010; Raghoebarsing et al., 2006) as well as metal oxides (Beal et al., 2009; Egger et al., 2015b; Riedinger et al., 2014; Scheller et al., 2016; Segarra et al., 2013; Sivan et al., 2011), sulfate ($SO_4^{2-}$) is commonly thought to be the dominant electron acceptor in anoxic marine systems (Knittel and Boetius, 2009; Reeburgh, 2007).

Nevertheless, a coupling between anaerobic $CH_4$ oxidation and iron (Fe) oxide reduction (Fe-AOM) could have a significant impact on sedimentary Fe cycling and related processes such as phosphorus (P) diagenesis, because of the 8:1 Fe-$CH_4$ stoichiometry of the reaction (Beal et al., 2009; Egger et al., 2015a; Rooze et al., 2016). Environmental conditions that favor Fe-AOM in marine systems are still poorly understood. The required co-occurrence of pore water $CH_4$ and abundant reducible Fe oxides suggests that Fe-AOM may occur in sediments that receive a relatively high input of Fe oxides compared to the in-situ production of sulfide, which could allow a portion of Fe oxides to escape the conversion to authigenic Fe sulfides and to remain preserved in the methanogenic sediments below the zone of $SO_4^{2-}$ reduction (Egger et al., 2015b; Riedinger et al., 2014; Rooze et al., 2016). In addition, perturbations inducing transient diagenesis such as anthropogenic eutrophication or climate change may also create diagenetic environments that are likely favorable for Fe-AOM, as they provide a mechanism for the burial of Fe oxide-rich deposits below sulfidic sediment layers (Egger et al., 2015b; Riedinger et al., 2014).

The Black Sea represents a good example of a sedimentary system in which transient diagenesis associated with postglacial sea-level rise has led to the accumulation of sulfidic sediments above Fe oxide-rich deposits. Here, the establishment of a connection to the Mediterranean Sea through the shallow Bosporus around 9000 years ago (Degens and Ross, 1974; Soulet et al., 2011) led to the inflow of marine waters into a freshwater basin, resulting in permanent salinity/density stratification and in the development of euxinic conditions (i.e. free dissolved sulfide present in the bottom water), making the current Black Sea the largest permanently anoxic basin on Earth.

In the absence of oxygen and metal oxides, $SO_4^{2-}$ reduction is the dominant benthic mineralization process of organic matter in Black Sea surface sediments below the chemocline (~ 100 m depth) (Jørgensen et al., 2001; Thamdrup et al., 2000). At present, $SO_4^{2-}$ penetrates through the modern coccolith ooze (Unit I) and the marine sapropel (Unit II) sediments and a few meters into the Upper Pleistocene freshwater deposits (Unit III) (Arthur and Dean, 1998; Degens and Ross, 1974; Jørgensen et al., 2004). Below the $SO_4^{2-}$-bearing zone, methanogenesis takes over as the dominant process of organic matter degradation, resulting in the buildup of $CH_4$ in the pore water at depth.

Interactions between the cycles of sulfur (S) and $CH_4$ in Black Sea sediments have been extensively studied during recent years (Holmkvist et al., 2011b; Jørgensen et al., 2001, 2004; Knab et al., 2009; Leloup et al., 2007) and AOM coupled to $SO_4^{2-}$ reduction ($SO_4$-AOM) was found to account for an estimated 7-18 % of total $SO_4^{2-}$ reduction in these sediments (Jørgensen et al., 2001). The production of sulfide in the sulfate-methane transition zone (SMTZ) as a result of $SO_4$-AOM represents the main source of pore water sulfide at depth in the sediment. This intensified production of sulfide drives an enhanced downward diffusive flux of sulfide into the deep limnic deposits of Unit III,

2

75   forming a distinct diagenetic sulfidization front recognized as a black band or a series of bands owing to the

76   conversion of Fe oxides to Fe sulfides (Berner, 1974; Jørgensen et al., 2004; Neretin et al., 2004).

77   At present, the impact of the downward-migrating sulfidization front on sedimentary P, a key nutrient for marine

78   phytoplankton, and the potential role of Fe-mediated AOM in the deep limnic deposits remain largely unknown. A

79   buildup of ferrous Fe ($Fe^{2+}$) in the pore water at depth as found in previous studies (Holmkvist et al., 2011b;

80   Jørgensen et al., 2004; Knab et al., 2009), could indicate ongoing Fe reduction in the $CH_4$-bearing deep limnic

81   sediments and thus a potential coupling between AOM and Fe oxide reduction. The sediment records investigated up

82   to now, however, do not extend deep enough to allow the sedimentary cycling of Fe and related biogeochemical

83   processes below the sulfidization front to be investigated. In particular, the presence of abundant dissolved $Fe^{2+}$

84   combined with a potential release of pore water phosphate ($HPO_4^{2-}$) during reductive dissolution of Fe oxides may be

85   conducive to the formation of reduced Fe(II)-P minerals such as vivianite ($Fe_3(PO_4)_2*8H_2O$) below the sulfidization

86   front (Egger et al., 2015a; Hsu et al., 2014; März et al., 2008; Sivan et al., 2011). Post-depositional diagenetic

87   alterations as a result of downward sulfidization could therefore overprint burial records of P in the Upper

88   Pleistocene deposits.

89   In this study, we combine detailed geochemical analyses of the sediment and pore water with multicomponent

90   diagenetic modeling to study the diagenetic alterations below the lake-marine transition at two sites in the western

91   Black Sea. Focusing on the dynamics of S, Fe and P, we demonstrate that AOM coupled to $SO_4^{2-}$ reduction enhances

92   the downward sulfidization and associated dissolution of Fe oxides, Fe carbonates and vivianite, supporting earlier

93   findings of an $SO_4$-AOM enhanced downward sulfidization in Black Sea sediments (Jørgensen et al., 2001). Below

94   the sulfidization front, downward diffusing $HPO_4^{2-}$ precipitates as vivianite by reaction with the abundant dissolved

95   $Fe^{2+}$. We propose that organoclastic Fe oxide reduction, reactivation of less reactive Fe oxides by methanogens

96   (Sivan et al., 2016) and/or AOM coupled to the reduction of Fe oxides are the key processes explaining the high

97   concentrations of dissolved $Fe^{2+}$ at depth in the sediment. Trends in total S and P with depth are significantly altered

98   by the above-mentioned reactions, highlighting that diagenesis may strongly overprint burial records of these

99   elements below a lake-marine transition.


100   **2        Materials and methods**

101   **2.1        Sample collection**

102   **2.1.1        Gravity core sampling**

103   Sediment samples were taken at two slope sites in the western Black Sea during a cruise in June 2013 with R/V

104   Pelagia. Gravity cores containing ~ 7 m of sediment were collected at sites 4 (43°40.6' N, 30°7.5' E; 377 meters

105   below sea surface (mbss)) and 5 (43°42.6' N, 30°6.1' E; 178 mbss) (Fig. 1), both situated below the current

106   chemocline (~ 100 m water depth). The core liners were pre-drilled with 2 cm diameter holes in two rows of 10 cm

107   resolution on opposing sides of the tube, offset by 5 cm and taped prior to coring. Upon recovery, the liners were cut

108   into 1 m sections, transferred to a temperature-controlled container set at in-situ bottom water temperature (11 °C)

109  and secured vertically. Subsequently, the taped holes were cut open and a cut-off syringe was inserted horizontally

110  directly after opening each hole.

111  From one series of holes, 10 mL of wet sediment was extracted at 20 cm resolution and immediately transferred into

112  a 65 mL glass bottle filled with saturated NaCl solution for $CH_4$ analysis. The NaCl solution was topped up after

113  addition of the sample, ensuring that no air bubbles remained. Each bottle was sealed with a black rubber stopper and

114  a screw cap and was subsequently stored upside-down at room temperature. From the second series of holes, 20 mL

115  sediment was extracted at 20 cm resolution, sealed with parafilm that was tightly closed with an elastic band, and

116  directly inserted into a nitrogen ($N_2$)-purged glove box. Subsequently, the sediment was transferred into a 50 mL

117  centrifuge tube and centrifuged (4500 rpm; 30 min). The supernatant from each centrifuged sample was filtered

118  through 0.45 µm pore size disposable filters via 20 mL plastic syringes in the glove box and collected in 15 mL

119  centrifuge tubes. The sediment fraction was stored frozen (-20 °C) for solid phase analysis. Filtered pore water

120  samples were sub-sampled under $N_2$ for analysis of dissolved $HPO_4^{2-}$, ammonium ($NH_4^+$), dissolved inorganic

121  carbon (DIC), Fe, manganese (Mn), $SO_4^{2-}$ and sulfide ($\sum H_2S = H_2S + HS^-$) (see section 2.2) Additional samples of 10

122  mL of sediment were collected at approximately 50 cm resolution and transferred into pre-weighed 15 mL glass vials

123  to determine porosity from gravimetric water loss.

124  **2.1.2   Multicore sampling**

125  To sample the surface sediment, sediment cores (30-60 cm of sediment and at least 10 cm of overlying water) were

126  recovered using an octopus multicorer (core diameter 10 cm). After recovery, the cores were stoppered at the base

127  and at the top and immediately transported to a temperature-controlled container (11 °C). One multicore from each

128  cast was pre-drilled with 2 cm diameter holes in two rows at 10 cm resolution on opposing sides of the tube, offset

129  by 5 cm, and taped prior to coring. These holes were sampled for $CH_4$ as described for the gravity cores. Another

130  core was directly inserted into a $N_2$-purged glove box through an airtight hole in the base. A bottom water sample

131  was collected using a 20 mL plastic syringe and the remaining bottom water was removed with a Tygon tube.

132  Subsequently, the core was sliced anoxically with decreasing resolution at depth, i.e. 0.5 cm resolution for the first 0-

133  2 cm, 1 cm resolution between 2-10 cm, 2 cm resolution between 10-20 cm and 4 cm resolution for the rest of the

134  core (> 20 cm). For each slice a sub-sample was placed in a pre-weighed 15 mL glass vial for water content and solid

135  phase analysis and stored under $N_2$ in airtight jars at -20 °C. A second sub-sample was transferred to a 50 mL

136  centrifuge tube and centrifuged (4500 rpm; 30 min). Both the supernatant water from each centrifuged sample and

137  the bottom water sample were subsequently processed as described for the gravity cores.

138  Visual alignment of the pore water profiles from the multicores with those of the gravity cores showed that the first ~

139  20 to 30 cm of sediment was lost during long coring. At site 5, the sediment in the multicore consisted of a gray and

140  homogeneous turbidite below 1.5 cm depth. The depth for the gravity core at site 5 was thus corrected for the loss of

141  the marine deposits, which were previously reported to be about 50 cm thick at a site in close proximity to site 5

142  (43°42.63' N, 30°6.12' E; 181 mbss) (Jørgensen et al., 2004)

4

143 **2.2      Pore water subsampling**

144 A sub-sample of 0.5 mL was immediately transferred into a glass vial containing 1.5 mL of 8 M NaOH solution for

145 analysis of dissolved sulfide. Sub-samples for total dissolved Fe and Mn, which are assumed to represent Fe(II) and

146 Mn(II), were acidified with 10 µL 35 % suprapur HCl per mL of sub-sample. Note, however, that the dissolved (<

147 0.45 µm) Fe and Mn pools likely consist of a mixture of truly dissolved (aqueous), as well as organically complexed,

148 colloidal and nanoparticulate Fe and Mn species (Raiswell and Canfield, 2012). Another 1 mL of pore water for

149 $HPO_4^{2-}$ analysis was acidified with 4 µL 5 M HCl. Pore water $SO_4^{2-}$ was analyzed with ion chromatography (IC) in a

150 10-fold diluted sample (0.15 mL of pore water with 1.35 mL of de-oxygenated UHQ water). Sub-samples for DIC

151 analysis (0.5 mL) were collected in glass vials (4.9 mL) to which 4.4 mL of 25 g/L NaCl solution was added, making

152 sure that no headspace remained. Aliquots of the remaining pore water were used for the measurement of alkalinity

153 (determined onboard by titrating 1 mL of untreated sub-sample with 0.01 M HCl; results presented in the

154 Supplementary Information only) and $NH_4^+$. All sub-samples were stored at 4 °C and brought to room temperature

155 just before analysis. Subsampling for sulfide was performed immediately after filtration and all other subsampling

156 was performed within 4 hours of core recovery.

157 Pore water sub-samples for $HPO_4^{2-}$, DIC and sulfide were directly analyzed colorimetrically onboard on two separate

158 QuAAtro (SEAL Analytical, Germany) auto analyzers. $HPO_4^{2-}$ was measured at 880 nm after the formation of

159 molybdophosphate-complexes (Murphy and Riley, 1962). Samples for DIC were acidified online after being

160 oxidized by $H_2O_2$ and analyzed as described by Stoll et al. (2001). To keep the dissolved sulfide in the non-volatile

161 $HS^-$ form under alkaline conditions, 1.5 mL of 8 mM NaOH was added to the sulfide samples, which were

162 subsequently analyzed using the methylene blue method as described by Grasshoff (1969). Sub-samples for

163 dissolved Fe and Mn were analyzed onshore by ICP-OES (Perkin Elmer Optima 3000 Inductively Coupled Plasma -

164 Optimal Emission Spectroscopy). For the analysis of pore water $CH_4$, a volume of 10 mL $N_2$ was injected into the

165 $CH_4$ serum flasks (while a needle inserted through the septum allowed 10 mL of water to escape) to create a

166 headspace from which a subsample was collected with a gas-tight syringe. Subsequently, $CH_4$ concentrations were

167 determined in the home laboratory after injection into a Thermo Finnigan Trace GC gas chromatograph (Flame

168 Ionization Detector). $\delta^{13}C$-$CH_4$ and $\delta D$-$CH_4$ (D, deuterium) were analyzed by Continuous Flow Isotope Ratio Mass

169 Spectrometry (CF-IRMS) as described in detail in (Brass and Röckmann, 2010) and (Sapart et al., 2011).

170 **2.3      Bulk sediment analysis**

171 Sediment samples were freeze-dried, powdered and ground in an agate mortar in an argon (Ar)-filled glove box and

172 split into oxic and anoxic fractions. Samples from the oxic fraction were used for total elemental and organic carbon

173 ($C_{org}$) analyses under normal atmospheric conditions, whereas anoxic splits for sediment P and Fe speciation were

174 kept under an inert, oxygen-free Ar or $N_2$ atmosphere at all times to avoid oxidation artefacts (Kraal and Slomp,

175 2014; Kraal et al., 2009).

5

### 2.3.1 Total elemental composition and organic carbon

A split of ~ 125 mg of freeze-dried sediment was dissolved overnight in 2.5 mL HF (40 %) and 2.5 mL of $HClO_4/HNO_3$ mixture, in a closed Teflon bomb at 90 °C. The acids were then evaporated at 160 °C and the resulting gel was dissolved overnight in 1 M $HNO_3$ at 90 °C. Total elemental concentrations in the 1 M $HNO_3$ solutions were determined by ICP-OES. A second split of 0.3 g freeze-dried sediment was used to determine the $C_{org}$ content using an elemental analyzer (Fison Instruments model NA 1500 NCS) after carbonate removal from the sediment with two washes with 1 M HCl (4 h and 12 h) followed by two washes with UHQ water and subsequent drying of the samples (Van Santvoort et al., 2002).

### 2.3.2 Sediment P fractionation

To determine the solid phase partitioning of P, aliquots of 0.1 g dried sediment were subjected to the SEDEX sequential extraction procedure after Ruttenberg (1992), as modified by Slomp et al. (1996b), but including the first $MgCl_2$ step (Table 1). Sediment P was fractionated as follows: i) exchangeable-P ("$P_{exch}$", extracted by 1 M $MgCl_2$, pH 8, 0.5 h), ii) Fe-associated P ("$P_{Fe}$", extracted by citrate-bicarbonate-dithionite (CDB), buffered to pH 7.5 with Na citrate/Na bicarbonate, 8 h, followed by 1 M $MgCl_2$, pH 8, 0.5 h), iii) authigenic Ca-P ("$P_{authi\ Ca-P}$", including carbonate fluorapatite, biogenic hydroxyapatite and $CaCO_3$-bound P, extracted by 1 M Na acetate solution, buffered to pH 4 with acetic acid, 6 h, followed by 1 M $MgCl_2$, pH 8, 0.5 h), iv) detrital Ca-P ("$P_{detr}$", extracted by 1 M HCl, 24 h) and v) organic P ("$P_{org}$", after ashing at 550 °C for 2 h, extracted by 1 M HCl, 24 h). The $MgCl_2$ washes in steps ii and iii were to ensure that any $HPO_4^{2-}$ re-adsorbed during CDB or acetate extraction was removed and included in the pools of Fe-associated P and authigenic Ca-P, respectively. Sediments were shielded from oxygen inside an Ar-filled glovebox until step 3 of the SEDEX procedure to eliminate the potential conversion of Ca-P to Fe-bound P due to pyrite oxidation upon oxygen exposure (Kraal and Slomp, 2014; Kraal et al., 2009). Dissolved $HPO_4^{2-}$ in the CDB solution was analyzed by ICP-OES. For all other solutions, $HPO_4^{2-}$ was determined colorimetrically (Strickland and Parsons, 1972) on a Shimadzu spectrophotometer using the ammonium heptamolybdate – ascorbic acid method.

### 2.3.3 Sediment Fe fractionation

Sediment Fe was fractionated into i) carbonate associated Fe ("$Fe_{carb}$", including siderite and ankerite, extracted by 1 M Na-acetate brought to pH 4.5 with acetic acid, 24 h), ii) easily reducible (amorphous) oxides ("$Fe_{ox1}$", including ferrihydrite and lepidocrocite, extracted by 1 M hydroxylamine-HCl, 24 h), iii) reducible (crystalline) oxides ("$Fe_{ox2}$", including goethite, hematite and akagenéite, extracted by Na-dithionite buffer, pH 4.8, 2 h) and iv) Fe in recalcitrant oxides (mostly magnetite, "$Fe_{mag}$", extracted by 0.2 M ammonium oxalate / 0.17 M oxalic acid solution, 2 h), according to Poulton and Canfield (2005), using a 50 mg aliquot of dried sediment (Table 1). An additional aliquot of 50 mg was subjected to an adapted sequential extraction procedure after Claff et al. (2010), separating labile Fe(II) ("$Fe(II)_{HCl}$") and Fe(III) ("$Fe(III)_{HCl}$") using 1 M HCl (4 h) from crystalline Fe oxide minerals ("$Fe(II)_{CDB}$", Na-dithionite buffer, pH 4.8, 4 h) and from pyrite ("$Fe_{pyrite}$", concentrated nitric acid, 2 h), for all multicores as well as for the long core at site 4 (Table 1).

6

211 At site 4 (multicore only) and 5 (multicore and gravity core), aliquots of 0.5 g dried sediment were used to

212 sequentially determine the amount of FeS (acid volatile sulfur, "AVS", using 6 M HCl) and $FeS_2$ (chromium

213 reducible sulfur, "CRS", using acidic chromous chloride solution) via the passive diffusion method described by

214 (Burton et al., 2008) using iodometric titration of the ZnS formed in the alkaline Zn acetate traps to quantify AVS

215 and CRS (Table 1).

216 **2.4    Diagenetic model**

217 **2.4.1    General form**

218 A multicomponent transient diagenetic model was developed for site 4 based on existing diagenetic models (Reed et

219 al., 2011a, 2011b; Rooze et al., 2016) to gain a better understanding of the transient diagenesis in Black Sea

220 sediments and to investigate the potential for Fe-AOM as a source of pore water $Fe^{2+}$ at depth. The model describes

221 the cycling of dissolved and particulate chemical species in a 1D sediment column (Berner, 1980). A total of 25

222 different chemical species (Table 2) were subjected to a suite of biogeochemical reactions (Table 3) and vertical

223 transport through burial, as well as molecular diffusion for dissolved species (Boudreau, 1997; Soetaert et al., 1996;

224 Wang and Van Cappellen, 1996). The general diagenetic equations for solid (Eq. (1)) and dissolved species (Eq. (2))

225 are, respectively,

226 $$(1 - \phi)\frac{\partial C_S}{\partial t} = -(1 - \phi)v\frac{\partial C_S}{\partial x} + \sum R_S \qquad (1)$$

227 $$\phi \frac{\partial C_{aq}}{\partial t} = \phi D' \frac{\partial^2 C_{aq}}{\partial x^2} - \phi u \frac{\partial C_{aq}}{\partial x} + \sum R_{aq} \qquad (2)$$

228 where $C_S$ is the concentration of the solid species (mol $L^{-1}$; mass per unit volume of solids), $C_{aq}$ the concentration of

229 the dissolved species (mol $L^{-1}$; mass per unit volume of pore water), t is time (yr), $\phi$ the sediment porosity, x the

230 distance from the sediment-water interface (cm), $D'$ the diffusion coefficients of dissolved species in the sediment

231 ($cm^2$ $yr^{-1}$) adjusted for the considered setting (Supplementary Table S1) (Boudreau, 1997) and corrected for the

232 tortuosity in the porous medium (Boudreau, 1996) (see Supplementary Information). $\sum R_S$ and $\sum R_{aq}$ are the net

233 reaction rates of the solid and dissolved species from the chemical reactions they participate in (Table 3), and $v$ and

234 $u$ the advective velocities (cm $yr^{-1}$) of the solid and the dissolved species, respectively. Porosity and advective

235 velocities were described by depth-dependent functions to account for sediment compaction (Meysman et al., 2005;

236 Reed et al., 2011a) (see Supplementary Information and Supplementary Fig. S1).

237 Reactions considered by the model and corresponding reaction equations are given in Tables 3 and 4, respectively,

238 and are divided into primary redox reactions and other biogeochemical reactions, including various mineral

239 formation and dissolution reactions (Reed et al., 2011a, 2011b; Rooze et al., 2016). Corresponding reaction

240 parameters were mostly taken from the literature or, if these were not available or no fit to the data could be obtained

241 with existing parameter ranges, constrained using the extensive geochemical dataset for site 4 (Table 5). A model

242 sensitivity analysis for key parameters is provided in the Supplementary Information (Supplementary Figs. S2 and

243 S3).

244 To account for differences in reactivity and crystallinity between different species, organic matter and Fe oxides are

245 divided into three different pools, representing highly reactive (α), less reactive (β) and non-reactive (i.e. inert) (γ)

7

246    phases. For the Fe oxides, only the α phase is used by organoclastic Fe reduction (Table 3), while the β phase is also

247    used by Fe-AOM. This assumption was made to test whether the pore water and sediment profiles observed in the

248    Black Sea can be reproduced with Fe-AOM as the main Fe reduction pathway at depth. In addition, it allows an

249    assessment of the potential impact of Fe-AOM on sedimentary $CH_4$ cycling. Note that, as a consequence of the

250    exclusion of organoclastic Fe reduction at depth, the model results should not be interpreted as proof for Fe-AOM

251    but rather imply that it is a possible mechanism.

252    The succession of oxidants during organic matter decomposition (Froelich et al., 1979) is described by means of

253    Monod kinetics (Table 4), whereby those oxidants with the highest metabolic free energy yield are used

254    preferentially until they become limiting and the oxidant with the next highest energy yield is used (Berg et al., 2003;

255    Boudreau, 1996; Reed et al., 2011b; Rooze et al., 2016; Wang and Van Cappellen, 1996). Oxidants considered by the

256    model are (in descending order of energy yield) $O_2$, nitrate ($NO_3^-$), Fe oxides and $SO_4^{2-}$. Once these oxidants are

257    exhausted, organic matter remineralization occurs by methanogenesis. Corresponding limiting concentrations for the

258    oxidants are taken from (Reed et al., 2011a) (Table 5). In addition, an attenuation factor, Ψ, is used to slow down

259    anaerobic organic matter degradation through $SO_4^{2-}$ reduction and methanogenesis, thus allowing for better

260    preservation of organic matter under anoxic bottom water conditions (Moodley et al., 2005; Reed et al., 2011a,

261    2011b).

262    Cycling of S is simulated using five different chemical species, i.e. Fe monosulfides (FeS), pyrite ($FeS_2$), elemental S

263    ($S_0$), dissolved sulfide and pore water $SO_4^{2-}$ (Table 2), combined in a network of various biogeochemical reactions

264    (Table 3). The $CH_4$ cycle includes $CH_4$ production from organic matter and from DIC (i.e. $CO_2$), as well as $CH_4$

265    oxidation coupled to the reduction of $O_2$, $SO_4^{2-}$ and $Fe(OH)_3$ (Table 3). For AOM a bimolecular rate equation was

266    used (Table 4), which is the most common way to parameterize AOM in reactive transport models (Regnier et al.,

267    2011) and allows the use of largely unknown half-saturation constants, in particular for the putative Fe-AOM

268    pathway, to be avoided. Although Mn-oxides have also been suggested to be a thermodynamically favorable electron

269    acceptor for AOM (Beal et al., 2009), they were not included in the model because of the relatively low Mn

270    concentrations (~ 15 μmol $g^{-1}$ for total sedimentary Mn and < 30 μM for dissolved $Mn^{2+}$; Supplementary Fig. S2 and

271    S3) when compared to Fe and the likely presence of most of the Mn in the form of Mn-carbonates.

272    The P forms included in the model are pore water $HPO_4^{2-}$, authigenic Ca-P, organic P and detrital P, as well as Fe-

273    bound P, i.e. P associated with Fe oxides and P in vivianite (Table 2). The removal of dissolved $Fe^{2+}$ through

274    formation of the Fe minerals FeS, siderite ($FeCO_3$) and vivianite is also included in the model (Table 3). Mass

275    balances for all chemical species included in the model are given in Supplementary Table S2.

276    The boundary conditions at the sediment surface were specified as time-dependent depositional fluxes for the

277    particulate components and as fixed bottom water concentrations for the dissolved species, while a zero gradient

278    boundary condition was set for all chemical species at the base of the model domain (Fig. 2 and Supplementary

279    Table S3). To avoid potential interferences of the lower boundary conditions with the model results in the upper

280    sediments (see Supplementary Fig. S6), the model depth was set to 3000 cm and divided into 500 grid cells. The

281    thickness of the upper layer was set at 1 cm, and the thickness of the following grid layers increased exponentially to

282    ~ 6 cm at 800 cm depth and to ~18 cm at 3000 cm depth. In this paper, only the upper 800 cm are shown. However,

283    all profiles extending over the full depth range are provided in the Supplementary Information file (Supplementary

8

284  Fig. S5 and Fig. S7). The model code was written in R using the marelac geochemical dataset package (Soetaert et

285  al., 2010) and the ReacTran package (Soetaert and Meysman, 2012) to calculate the transport in porous media. The

286  set of ordinary differential equations was subsequently solved numerically with the lsoda integrator algorithm

287  (Hindmarsh, 1983; Petzoldt, 1983)

### 2.4.2    Transient scenario

289  The model applied in this study simulates the sediment deposition during the last 25000 years. A constant mass

290  accumulation rate of 0.06 g cm$^{-2}$ yr$^{-1}$ over the Holocene was assumed. In order to reduce the computing time for the

291  freshwater period, a higher mass accumulation rate of 1 g cm$^{-2}$ yr$^{-1}$ was used between 25000 and 10000 years before

292  present (B.P.) and all fluxes were corrected accordingly (i.e. multiplied with a factor of 16.67). Inflow of

293  Mediterranean saltwater into the Black Sea basin was modelled assuming an initial salinity of 1 for the freshwater

294  lake and a linear increase to a salinity of 22 between 8500 and 1500 years B.P. (Fig. 2). Such a salinization scenario

295  results in a good fit to the chloride (Cl$^-$) profile (Fig. 3) and compares well with a previous salinity reconstruction

296  suggesting a linear increase in salinity of 1 to 22 between 9000 ± 500 years B.P. and 2000 ± 500 years B.P. (Soulet et

297  al., 2010). Bottom water salinity was converted to Cl$^-$ and SO$_4^{2-}$ using the molecular weights and seawater density

298  derived from the marelac geochemical dataset package (Soetaert et al., 2010) (Supplementary Table S1). A shift

299  from oxic towards euxinic conditions around 7600 years B.P., with a peak in organic matter loading around 5300

300  years B.P. and constant elevated organic matter fluxes after 2700 years B.P. was assumed, following a recent study

301  comprising data from seven sediment cores collected from the Black Sea (Eckert et al., 2013) (Fig. 2). In addition,

302  the input of organic matter was assumed to increase again in the last century, reflecting anthropogenic eutrophication

303  of waters on the adjacent continental shelf as previously reported (Capet et al., 2013; Kemp et al., 2009). With the

304  development of anoxic and sulfidic bottom-water conditions, depositional fluxes of reactive Fe oxides were assumed

305  to be zero (Fig. 2). In contrast, fluxes of Fe sulfides are high under euxinic conditions and dominated by FeS$_2$.

### 3    Results

### 3.1    Pore water profiles

308  Pore water profiles of SO$_4^{2-}$ show a linear decrease from ~ 17 mM at the sediment water interface to a depth of ~ 230

309  cm at both sites, below which CH$_4$ starts to accumulate in the pore water (Fig. 3). Bubble formation and degassing of

310  CH$_4$ during gravity coring could not be avoided because of the high concentrations of CH$_4$ in the limnic deposits

311  above the saturation of ca 1.3 mM CH$_4$ at atmospheric pressure (calculated for a salinity of 22 and a temperature of

312  25 °C using the algorithm from Mogollón et al. (2013)). Observations of increased outgassing with depth during

313  coring suggest that the low CH$_4$ concentrations in the deeper sediments at both sites are due to enhanced outgassing

314  with increasing levels of CH$_4$. Pore water profiles of NH$_4^+$ at both sites are similar and concentrations increase to ~ 3

315  mM at depth, suggesting that actual CH$_4$ concentrations at both sites could be comparable. Most of the CH$_4$ values

316  thus only indicate the presence or absence of CH$_4$ and are not a quantitative measure (indicated as open diamonds in

317  Fig. 4). Note that the upper ~ 300 cm of sediment at site 5 are likely less affected by CH$_4$ outgassing. Modeled pore

318    water concentrations of $CH_4$ on the other hand, show a steep increase below the SMTZ, comparable to the gradient

319    observed at site 5, and build up to concentrations of ~ 15 mM at depth (Supplementary Fig. S5).

320    The SMTZ is located around 230 cm depth in the sediment and is characterized by the removal of both pore water

321    $SO_4^{2-}$ and dissolved $CH_4$. In this zone, $SO_4$-AOM drives the production of dissolved sulfide, DIC and alkalinity

322    (Supplementary Fig. S5) and diffusion of these pore water constituents away from the SMTZ (Fig. 3). Below the

323    sulfide diffusion front, $Fe^{2+}$ accumulates in the pore water. Dissolved $HPO_4^{2-}$ reaches a maximum around the depth

324    where sulfide levels drop below the detection limit of 1 $\mu$mol $L^{-1}$, followed by a steep decrease with depth.

325    Concentrations of pore water $Mn^{2+}$ are more than an order of magnitude lower than those of dissolved $Fe^{2+}$, and

326    decrease from the sediment surface until ~ 200 cm depth, below which they slightly increase again (Supplementary

327    Fig. S5).

328    The smooth pore water profiles of $\delta^{13}C$-$CH_4$ and $\delta D$-$CH_4$ suggest that the isotopic composition of pore water $CH_4$

329    (available for site 5 only) is less affected by the $CH_4$ loss and reveals a biological origin in the limnic deposits, with

330    hydrogenotrophic carbonate reduction, i.e. microbial reduction of $CO_2$ to $CH_4$ as the main methanogenic pathway for

331    the range of $CH_4$ isotope ratios observed in these sediments (Fig. 4) (Whiticar, 1999). Upward diffusing $CH_4$ shows a

332    gradual depletion in $\delta^{13}C$-$CH_4$ from ~ -74 ‰ at depth to ~ -96 ‰ around the SMTZ, followed by subsequent

333    progressive $^{13}C$ enrichment towards the sediment surface. $\delta D$-$CH_4$ shows a small enrichment from -226 ‰ at depth

334    to ~ -208 ‰ at the SMTZ and a strong shift towards high $\delta D$-$CH_4$ values of up to ~ 113 ‰.

335    **3.2    Solid phase profiles**

336    A pronounced excursion in sedimentary $C_{org}$ at site 4 in combination with a shift from gray clay deposits to micro-

337    laminated black sediments indicates that the lake-marine transition, i.e. the transition between the marine sapropel

338    Unit II and the deep limnic sediments of Unit III (Arthur and Dean, 1998; Degens and Ross, 1974), is located around

339    a sediment depth of ~ 90 cm at site 4 (Fig. 5). At site 5, Unit I and Unit II were lost due to a turbidite, explaining the

340    low concentrations of $C_{org}$ in the upper sediments.

341    Concentrations of solid S increase with decreasing depth from 20 $\mu$mol $g^{-1}$ below 300 cm (sulfidization front) to ~

342    400 $\mu$mol $g^{-1}$ in the upper 100 cm at both sites and are dominated by $FeS_2$ (Fig. 5). Iron oxides show a decrease from

343    ~ 100 $\mu$mol $g^{-1}$ at depth to ~ 50 $\mu$mol $g^{-1}$ in the sediments between 100 – 300 cm and a further decrease to ~ 10 $\mu$mol

344    $g^{-1}$ closer to the sediment surface. Amorphous Fe oxides ($Fe_{ox1}$) and more crystalline oxides ($Fe_{ox2}$) both account for

345    half the total amount of Fe oxides, with a small contribution of recalcitrant oxides ($Fe_{mag}$) (Supplementary Fig. S4).

346    The results from the two different Fe extractions applied in this study (Table 1) generally compare well

347    (Supplementary Fig. S4). Note, however, that the Fe oxides in Fig. 5 represent the results from the extraction after

348    Poulton and Canfield (2005). Results from the Fe extractions modified from Claff et al. (2010) are provided in the

349    Supplementary Information only. Sedimentary Mn content is relatively low at all three sites, ranging from ~ 5-10

350    $\mu$mol $g^{-1}$ in the marine sediments to ~ 15 $\mu$mol $g^{-1}$ in the deep limnic deposits of Unit III (Supplementary Fig. S4).

351    Sediments below the sulfidization front are characterized by high Fe carbonate contents of ~ 100 $\mu$mol $g^{-1}$. The sharp

352    depletion in Fe carbonate around the sulfidization front could only be reproduced in the model by assuming Fe

353 carbonate dissolution by dissolved sulfide (Table 3). These results suggest a conversion of reactive Fe from

354 carbonate toward sulfide phases in the presence of abundant dissolved sulfide.

355 Units I and II show high concentrations of organic P, which accounts for $\sim$ 30 % of total P in these sediments (Fig.

356 5). Low organic P and high concentrations of detrital P in the upper sediments at site 5 are due to the turbidite. The

357 limnic deposits of Unit III are generally depleted in organic P (< 6 % of total P) and enriched in detrital P.

358 Authigenic Ca-P shows little variation in the sediments of Unit III, accounting for $\sim$ 20 to 30 % of total P at the two

359 sites. The contribution of Fe-associated P, on the other hand, is reduced in the limnic deposits of Unit III exposed to

360 the downward diffusing sulfide ($\sim$ 20 %) when compared to the sediments below the sulfidization front ($\sim$ 30 %).

361 Concentrations of exchangeable P are < 2 $\mu$mol g$^{-1}$ for sediments above the SMTZ and < 1 $\mu$mol g$^{-1}$ for sediments at

362 depth (data not shown).

363 Modeled $SO_4^{2-}$ reduction rates show two distinct peaks of $\sim$ 200 pmol $SO_4^{2-}$ cm$^{-3}$ d$^{-1}$ in the sediments of Unit II and

364 in the sediments around the SMTZ (Fig. 6). Rates of $CH_4$ production are highest ($\sim$ 30 pmol $CH_4$ cm$^{-3}$ d$^{-1}$) in the

365 organic-rich marine deposits of Unit II and in the limnic deposits below the SMTZ. The sediments around the SMTZ

366 are further characterized by high rates of $SO_4$-AOM ($\sim$ 200 pmol cm$^{-3}$ d$^{-1}$), whereas sediments directly below the

367 sulfidization front show enhanced rates of $S_0$ disproportionation ($\sim$ 15 pmol cm$^{-3}$ d$^{-1}$). Organoclastic $SO_4^{2-}$ reduction

368 provides the main source for pore water sulfide in the organic-rich marine deposits, while $SO_4$-AOM and $S_0$

369 disproportionation are the dominant sources of dissolved sulfide in sediments around the SMTZ and directly below

370 the sulfidization front, respectively. Rates of Fe-AOM are generally low (< 0.04 pmol $CH_4$ cm$^{-3}$ d$^{-1}$) and restricted to

371 the limnic deposits only.

372 **3.3 Temporal evolution**

373 The temporal evolution in pore water and solid phase constituents illustrates the impact of the lake-marine transition

374 on the sediment geochemistry (Fig. 7). Concentrations of pore water Cl$^-$ and $SO_4^{2-}$ increase with the intrusion of

375 marine Mediterranean Sea waters, accompanied by a decrease in dissolved $CH_4$ and accumulation of pore water

376 sulfide in the shallower sediments. Dissolved $Fe^{2+}$ becomes restricted to non-sulfidic pore waters at depth, while

377 $HPO_4^{2-}$ and solid S start to accumulate in the presence of dissolved sulfide. Iron oxides decrease in the surface

378 sediments as well as in the sediments at depth. Vivianite, on the other hand, becomes increasingly enriched in

379 sediments below the downward diffusing sulfide front.

380 **4. Discussion**

381 **4.1 Coupled S, $CH_4$ and Fe dynamics**

382 **4.1.1 Organoclastic $SO_4^{2-}$ reduction**

383 Model-derived areal rates of total $SO_4^{2-}$ reduction of $\sim$ 0.24 mmol $SO_4^{2-}$ m$^{-2}$ d$^{-1}$ (Table 6), i.e. the total amount of

384 $SO_4^{2-}$ reduced per square meter of sea floor, compare well with calculated diffusive fluxes of $SO_4^{2-}$ into the sediment

385 at sites 4 and 5 ($\sim$ 0.21 and 0.20 mmol $SO_4^{2-}$ m$^{-2}$ d$^{-1}$, respectively) and are in good agreement with previous $SO_4^{2-}$ flux

386 estimates of 0.17 to 0.28 mmol $SO_4^{2-}$ m$^{-2}$ d$^{-1}$ for sediments of the western Black Sea (Jørgensen et al., 2001). In the

11

387  model, organoclastic $SO_4^{2-}$ reduction accounts for > 65 % of total organic matter degradation in the upper 800 cm of

388  sediment, supporting previous conclusions that $SO_4^{2-}$ reduction represents the dominant mineralization process of

389  organic matter in sediments below the chemocline (Jørgensen et al., 2001; Thamdrup et al., 2000). The remaining <

390  25 % of organic matter remineralization is due to methanogenesis. The relative contribution of SRR to organic

391  matter remineralization, however, likely is significantly higher when taking into account the high SRR in the

392  uppermost sediment layers (Jørgensen et al., 2001), which are not captured by our model.

393  The depth-dependent rate profile of $SO_4^{2-}$ reduction shows two distinct peaks of ~ 70 and 230 pmol $SO_4^{2-}$ $cm^{-3}$ $d^{-1}$

394  associated with organoclastic $SO_4^{2-}$ reduction in the organic matter rich marine deposits of Unit I and Unit II. These

395  rates are at the low end of reported values from Black Sea sediments (0.1 - 20 nmol $cm^{-3}$ $d^{-1}$) (Holmkvist et al.,

396  2011b; Jørgensen et al., 2001, 2004; Knab et al., 2009; Leloup et al., 2007). Our model further demonstrates that the

397  two SRR peaks in the sediments of Unit I and Unit II are not reflected in the pore water profile of $SO_4^{2-}$. This finding

398  is in line with earlier work showing that the $SO_4^{2-}$ gradient in Black Sea sediments is primarily affected by $SO_4$-

399  AOM in the SMTZ (Jørgensen et al., 2001). The shorter diffusion distance (the diffusion time to ~ 200 cm is about 5

400  times longer than to ~ 90 cm, i.e. ~ 300 years vs. ~ 60 years) and higher porosity in Unit I and II (Supplementary Fig.

401  S1) both dampen the effect of $SO_4^{2-}$ reduction in the marine deposits on the $SO_4^{2-}$ profile (see also Jørgensen et al.,

402  (2001)). Thus, our results support previous conclusions that SRR estimates based on pore water profiles of $SO_4^{2-}$ (i.e.

403  net $SO_4^{2-}$ consumption) alone may underestimate the actual $SO_4^{2-}$ turnover (i.e. gross $SO_4^{2-}$ reduction) in marine

404  sediments (Jørgensen, 1978; Jørgensen et al., 2001).


405  **4.1.2 $SO_4$-AOM**

406  Pore water profiles of $SO_4^{2-}$, $CH_4$, sulfide and DIC reveal a distinct SMTZ around 230 cm depth at both sites, where

407  $SO_4$-AOM with upward diffusing $CH_4$ results in the concomitant removal of pore water $SO_4^{2-}$ and $CH_4$ and in the

408  accumulation of dissolved sulfide and DIC in the pore waters of these sediments (Fig. 3). The depth of the SMTZ

409  and the steep increase in $CH_4$ to > 3 mM below the SMTZ found in this study are consistent with earlier observations

410  in sediments of the western Black Sea (Henkel et al., 2012; Holmkvist et al., 2011b; Jørgensen et al., 2001, 2004;

411  Knab et al., 2009; Leloup et al., 2007). The location of the SMTZ, however, has progressed downwards in the last ca.

412  9000 years, following the inflow of $SO_4^{2-}$-rich salt water into the Black Sea basin (Fig. 7) (see also Henkel et al.,

413  (2012)).

414  Calculated diffusive fluxes of $SO_4^{2-}$ and $CH_4$ to the SMTZ (~ 0.2 mmol $SO_4^{2-}$ $m^{-2}$ $d^{-1}$ and 0.08 mmol $CH_4$ $m^{-2}$ $d^{-1}$) and

415  modelled areal rates of $SO_4$-AOM (~ 0.16 mmol $m^{-2}$ $d^{-1}$) suggest that AOM accounts for ~ 40 to 70 % of the total

416  $SO_4^{2-}$ reduction in these sediments, with the remaining ~ 30 to 60 % attributed to organoclastic $SO_4^{2-}$ reduction. Such

417  a high contribution of AOM exceeds the range of previous estimates that included experimentally measured SRR

418  close to the sediment surface (~ 7 to 18 %) (Jørgensen et al., 2001, 2004). Around the SMTZ, $SO_4$-AOM is

419  responsible for ~ 97 % of the total $SO_4^{2-}$ reduction (Fig. 6 and Table 6), thus enhancing the downward diffusive flux

420  of sulfide into the deep limnic deposits of Unit III. Our model suggests that without this additional source of sulfide

421  through $SO_4$-AOM, the sulfidization front would currently be located around 150 cm depth in the sediment (Fig. 8).

12

422 The consumption of upward diffusing $CH_4$ by $SO_4^{2-}$-driven AOM leads to a progressive enrichment of $^{13}C$ and D in

423 the residual $CH_4$ above the SMTZ (Fig. 4) due to the preferential oxidation of isotopically light $CH_4$ during $SO_4$-

424 AOM (Alperin et al., 1988; Martens et al., 1999; Whiticar, 1999). Interestingly, pore water $CH_4$ above the SMTZ

425 shows unusually high $\delta D$-$CH_4$ values that fall outside of the common range observed for pore water $\delta D$-$CH_4$ (e.g.

426 Whiticar et al., 1999). Future studies, however, are needed to resolve the cause of the strong D-enrichment of

427 dissolved $CH_4$ above the SMTZ in Black Sea sediments.

428 Modeled concentrations of $CH_4$ indicate that the measurements above the sulfidization front at site 5 are likely less

429 affected by outgassing during core recovery (Fig. 4) and can thus be used to derive kinetic isotope fractionation

430 factors for carbon ($\varepsilon_C$) and hydrogen ($\varepsilon_H$) associated with $SO_4$-AOM at the SMTZ using the Rayleigh distillation

431 function (Crowe et al., 2011; Egger et al., 2015b; Rayleigh, 1896; Whiticar, 1999). Corresponding estimates for $\varepsilon_C$ of

432 ~ 8 ‰ ($R^2 = 0.972$) and $\varepsilon_H$ of ~ 58 ‰ ($R^2 = 0.982$) are at the lower end of previously documented values in marine

433 and brackish-marine environments (8-38 ‰ for $\varepsilon_C$ and 100-324 ‰ for $\varepsilon_H$) (Alperin et al., 1988; Egger et al., 2015b;

434 Holler et al., 2009; Martens et al., 1999; Reeburgh, 2007). Note, however, that the Rayleigh distillation function only

435 applies to closed systems (Rayleigh, 1896). These estimates should therefore be interpreted as an approximation, as

436 more accurate estimates would require isotope modeling (e.g. Alperin et al., 1988).

437 At the base of the SMTZ, upward diffusing $CH_4$ reveals an initial depletion in $\delta^{13}C$-$CH_4$ (Fig. 4). Such a shift to $^{13}C$-

438 depleted $CH_4$ together with a decrease in its concentration could indicate an enzyme-mediated equilibrium C isotope

439 exchange during $SO_4$-AOM at low $SO_4^{2-}$ concentrations (< 0.5 mM) (Holler et al., 2012; Yoshinaga et al., 2014). The

440 effect of such mechanisms on deuterated $CH_4$ is likely limited.

441 **4.1.3 Cryptic S cycling**

442 Earlier studies showed evidence for ongoing $SO_4^{2-}$ reduction (< 1 nmol cm$^{-3}$ d$^{-1}$) within the $SO_4^{2-}$-depleted (< 0.5

443 mM) limnic deposits below the SMTZ in sediments of the Black Sea (Holmkvist et al., 2011b; Knab et al., 2009;

444 Leloup et al., 2007), Baltic Sea (Holmkvist et al., 2011a, 2014; Leloup et al., 2009) and Alaskan Beaufort Sea

445 (Treude et al., 2014) likely driven by $SO_4^{2-}$ production from re-oxidation of dissolved sulfide with oxidized Fe

446 minerals. In this mechanism, Fe oxides enhance the recycling of sulfide to $SO_4^{2-}$ in a cryptic S cycle (Holmkvist et

447 al., 2011a; Treude et al., 2014) thereby fueling $SO_4^{2-}$-driven AOM in Fe oxide-rich sediments. In this cryptic S cycle,

448 dissolved sulfide is oxidized to zero-valent sulfur ($S_0$), a key intermediate in AOM, which is subsequently

449 disproportionated to $SO_4^{2-}$ and sulfide by associated Deltaproteobacteria (Holmkvist et al., 2011a; Milucka et al.,

450 2012; Sivan et al., 2014; Treude et al., 2014). The additional $SO_4^{2-}$, produced during $S_0$ disproportion, may then

451 be re-used by the methanotrophic archaea as an electron acceptor for $SO_4$-AOM (Milucka et al., 2012).

452 Our model results suggest slow rates of ongoing $SO_4^{2-}$ reduction of < 0.2 nmol cm$^{-3}$ d$^{-1}$ (Fig. 6) within the limnic

453 deposits below the SMTZ exposed to dissolved sulfide (Table 6), in line with estimated SRR based on $^{35}SO_4^{2-}$

454 incubation experiments with Black Sea sediments from below the SMTZ of ~ 0.1-0.5 nmol cm$^{-3}$ d$^{-1}$ (Knab et al.,

455 2009; Leloup et al., 2007). Below the sulfidization front, SRR show a distinct peak of ~ 5 pmol cm$^{-3}$ d$^{-1}$. Active $SO_4^{2-}$

456 reduction in these $SO_4^{2-}$-depleted sediments requires deep $SO_4^{2-}$ formation to maintain low net rates of $SO_4^{2-}$

457 reduction. In the model, $S_0$ disproportionation is the only potential source of pore water $SO_4^{2-}$ at depth (Table 3).

13

458    Formation of $S_0$, in turn, occurs exclusively by oxidation of dissolved sulfide during the reductive dissolution of Fe

459    oxides, explaining the distinct $S_0$ disproportionation peak of $\sim$ 15 pmol cm$^{-3}$ d$^{-1}$ around the sulfidization front (Fig. 6).

460    Thus, based on the model assumptions, we conclude that Fe oxides increase the transformation of sulfide to $SO_4^{2-}$ via

461    formation and subsequent disproportionation of $S_0$ in these sediments, as suggested previously (Holmkvist et al.,

462    2011b; Knab et al., 2009; Leloup et al., 2007). Such recycling of $SO_4^{2-}$ stimulates slow rates of $SO_4$-AOM in the

463    sediments below the SMTZ, explaining the low background rates of $SO_4^{2-}$ reduction in the $SO_4^{2-}$-depleted limnic

464    deposits. These results support recent findings of indirect Fe stimulated $SO_4^{2-}$ driven AOM in laboratory experiments

465    (Sivan et al., 2014), and highlight that Fe oxides could play a significant role as stimulators of AOM and S recycling

466    in natural environments.

467    **4.2 Fe reduction below the sulfidization front**

468    Below the sulfidization front, $Fe^{2+}$ starts to accumulate in the pore water (Fig. 3). Although previous studies have

469    also reported an increase of dissolved $Fe^{2+}$ around the depth where sulfide levels drop below the detection limit

470    (Holmkvist et al., 2011b; Jørgensen et al., 2004; Knab et al., 2009), the source of this pore water $Fe^{2+}$ has remained

471    unknown. One possible explanation could be that the elevated $Fe^{2+}$ concentrations at depth represent remnant $Fe^{2+}$

472    accumulated during the Black Sea "Lake" phase (Knab et al., 2009). In our model, $Fe^{2+}$ shows a broad peak of $\sim$ 300

473    µM until $\sim$ 300 cm depth in the sediment during the initial Lake phase, assuming organoclastic Fe reduction as the

474    only Fe reduction pathway (data not shown). The removal of $Fe^{2+}$ through authigenic formation of reduced Fe(II)

475    minerals, however, prevents the accumulation of substantial amounts of $Fe^{2+}$ in the pore water below $\sim$ 300 cm

476    sediment depth during the Lake phase (Fig. 8). We therefore conclude that the high concentrations of dissolved $Fe^{2+}$

477    below the sulfidization front are most likely indicative of active Fe reduction in these sediments.

478    **4.2.1 Fe reduction through cryptic S cycling**

479    In theory, a cryptic S cycle, as described in section 4.1.3, could result in net accumulation of dissolved $Fe^{2+}$ if the

480    sulfide consumption from reaction with ferric Fe outweighs the production of sulfide from $SO_4^{2-}$ reduction. Modeled

481    $Fe^{2+}$ indeed shows a peak of < 100 µM directly below the sulfidization front, assuming no active Fe reduction in the

482    limnic deposits (Fig. 8). Model simulations further indicate that, based on the reaction network used in this study

483    (Table 3), cryptic S cycling could result in a build up of pore water $Fe^{2+}$ of $\sim$ 300 µM at depth in the sediment

484    provided there was no precipitation of reduced Fe(II) minerals (Supplementary Fig S2). However, concentrations of

485    dissolved $Fe^{2+}$ are too low compared to the measurements and confined to sediments between 300 – 400 cm depths

486    only. The diagenetic model developed in this study therefore suggests that cryptic S cycling is unlikely to explain the

487    high concentrations ($\sim$ 800 µM) of dissolved $Fe^{2+}$ observed in the deep limnic deposits.

488    **4.2.2 Organoclastic Fe reduction**

489    In the model, the reduction of Fe oxides coupled to organic matter degradation only occurs with the easily reducible

490    α phase in order to allow for the burial of the more crystalline β phase at depth (Table 3). Since the α phase is

491    efficiently reduced in the upper few centimeters during organoclastic Fe reduction, no easily reducible Fe oxides are

14

492    being buried into the deep sediments in the diagenetic model. Organoclastic Fe reduction therefore does not occur

493    within the modeled deep limnic deposits that exclusively contain more crystalline (β) and refractory (γ) Fe oxides

494    (Fig. 5). Instead, we assume that $CH_4$ represents a plausible electron donor for the reduction of more crystalline Fe

495    oxides in the organic-poor deep sediments with relatively refractory old organic matter (< 0.8 wt %). The exclusion

496    of organoclastic Fe reduction at depth in the model provides an estimate of an upper constraint on the potential

497    importance of Fe-AOM in Black Sea sediments. As a result of this assumption, however, the model results cannot be

498    used to conclude whether Fe-AOM is more likely than organoclastic Fe reduction.

499    An increasing body of geochemical evidence and laboratory incubation experiments shows that Fe-AOM might be

500    occurring in a variety of different aquatic environments (Amos et al., 2012; Beal et al., 2009; Crowe et al., 2011;

501    Egger et al., 2015b; Riedinger et al., 2014; Scheller et al., 2016; Segarra et al., 2013; Sivan et al., 2011; Wankel et

502    al., 2012). In addition, several studies have shown that Fe-reducing microorganisms are able to outcompete

503    methanogens for common substrates (e.g. acetate and $H_2$), thus reducing the concentrations of these common

504    primary electron donors to levels that are too low for methanogens to grow (Achtnich et al., 1995; Lovley and

505    Phillips, 1987; Lovley et al., 1989). These results, together with the observed capability of methanogens to switch

506    from $CH_4$ production to Fe reduction (Bodegom et al., 2004; Bond and Lovley, 2002; Liu et al., 2011; Reiche et al.,

507    2008; Sivan et al., 2016; Vargas et al., 1998) led to the common conclusion that Fe oxides exert a suppressive effect

508    on methanogenesis. Ongoing $CH_4$ production in the Fe oxide-rich limnic deposits, as deduced from the isotopic

509    composition of pore water $CH_4$ (Fig. 4) could then indicate limited organoclastic Fe reduction in these sediments.

510    However, there is increasing evidence that (semi)conductive crystalline Fe oxides (e.g. hematite and magnetite) can,

511    in fact, stimulate concurrent methanogenesis and organoclastic Fe reduction through direct interspecies electron

512    transfer (DIET), by serving as electron conduits among syntrophic $CH_4$-producing organisms at rates that are

513    substantially higher than those for interspecies electron transfer by $H_2$ (Cruz Viggi et al., 2014; Kato et al., 2012; Li

514    et al., 2014; Zhou et al., 2014; Zhuang et al., 2015). The inhibitory effect of Fe reduction on methanogenesis thus

515    appears to be lower for crystalline Fe oxides such as hematite and magnetite, which are less bioavailable to Fe-

516    reducing organisms than poorly crystalline (amorphous) Fe oxides (e.g. ferrihydrite and lepidocrocite) (Lovley,

517    1991; Qu et al., 2004; Zhuang et al., 2015). These findings indicate that the crystallinity and conductivity of Fe

518    oxides may play a key role in determining whether methanogenesis is stimulated or suppressed in Fe oxide-rich

519    environments. In addition, the presence of methanogens that are able to rapidly switch between methanogenesis and

520    reduction of Fe oxides could also result in a reactivation of less reactive Fe oxides that were not reduced during

521    initial organoclastic Fe reduction in the deep methanogenic zone as suggested by Sivan et al. (2016). Thus, the deep

522    limnic sediments may be characterized by a complex interplay of concurrent methanogenesis, Fe oxide reduction and

523    methanotrophy, i.e. AOM.


524    **4.2.3 Fe-AOM**

525    Our model results indicate that Fe-AOM could also be a possible mechanism explaining the buildup of pore water

526    $Fe^{2+}$ below the sulfidization front. Previous studies have shown that in systems where production and oxidation of

527    $CH_4$ take place concurrently, methanogenesis might conceal the isotopic signature of AOM (Egger et al., 2015b;

15

528    Seifert et al., 2006; Whiticar, 1999). Thus, unlike $SO_4$-AOM, Fe-dependent AOM likely only has little effect on the

529    isotopic composition of pore water $CH_4$ due to the removal of small amounts of $CH_4$ in sediments with ongoing

530    methanogenesis. This might explain why pore water $CH_4$ does not show enrichment in both heavy isotopes below the

531    sulfidization front as would be expected if Fe-AOM would occur, but rather indicates antipathetic changes, i.e.

532    depletion in $^{13}C$-$CH_4$ and enrichment in D-$CH_4$, usually attributed to $CH_4$ production from carbonate reduction

533    (Chanton et al., 2005; Whiticar, 1999).

534    Model derived rates for Fe-AOM of ~ 0.04 pmol $cm^{-3}$ $d^{-1}$ (Fig. 6) are significantly lower than potential Fe-AOM

535    rates of ~ 4 nmol $cm^{-3}$ $d^{-1}$ estimated from laboratory incubation studies (Egger et al., 2015b; Segarra et al., 2013;

536    Sivan et al., 2011) with brackish and limnic sediment samples. This large deviation is likely due to an overestimation

537    of Fe-AOM rates derived from stimulated microbial communities under laboratory conditions using freshly

538    synthesized and thus easily bioavailable Fe oxides when compared to in-situ conditions.

539    In the upper 800 cm of sediment, Fe-AOM accounts for < 1 % of total $CH_4$ oxidation, with the remaining > 99 %

540    attributed to $SO_4$-AOM (Table 6; see also Supplementary Fig. S2). However, while high rates of $SO_4$-AOM are

541    mainly restricted to the SMTZ, Fe-AOM might occur over a deep methanogenic zone, reaching far down into the

542    sediment. To accurately assess the contribution of Fe-AOM to the total $CH_4$ consumption in Black Sea sediments,

543    additional knowledge about the vertical expansion of the Fe oxide-rich limnic sediments deposited during the Blake

544    Sea "Lake" phase would be required.

**4.3 Impact of S-Fe-$CH_4$ dynamics on sedimentary P diagenesis**

546    Degradation of organic matter and the subsequent release of $HPO_4^{2-}$ to the pore water during early diagenesis

547    typically results in a sink-switching from organic P to authigenic P-bearing phases such as Ca phosphates (Filippelli,

548    1997; Ruttenberg and Berner, 1993; Slomp et al., 1996b), Mn-Ca carbonates (Jilbert and Slomp, 2013; Mort et al.,

549    2010; Suess, 1979) or reduced Fe phosphates (Burns, 1997; Jilbert and Slomp, 2013; Martens et al., 1978; März et

550    al., 2008). Reductive dissolution of Fe oxides by dissolved sulfide and the following liberation of $HPO_4^{2-}$ may also

551    contribute to the buildup of pore water $HPO_4^{2-}$ (Burns, 1997; Egger et al., 2015a; März et al., 2008; Schulz et al.,

552    1994). Thus, the downward sulfidization ultimately results in the accumulation of dissolved $HPO_4^{2-}$ in the pore water

553    as the sulfidization front moves downward into the limnic deposits (Fig. 7).

554    The pore water profile of $HPO_4^{2-}$ (Fig. 3) indicates the presence of a sink for $HPO_4^{2-}$ below the sulfidization front

555    and, to a lesser extent, in the sulfidic sediments around the SMTZ, likely unrelated to Ca-P authigenesis (Fig. 5).

556    Such a sink for $HPO_4^{2-}$ below sulfidic sediments has been observed previously (Burns, 1997; Egger et al., 2015a;

557    März et al., 2008; Schulz et al., 1994; Slomp et al., 2013) and shown to be most likely the result of vivianite

558    formation (Egger et al., 2015a; Hsu et al., 2014; März et al., 2008). Abundant dissolved $Fe^{2+}$ and a peak in Fe-

559    associated P below the sulfidization front observed in this study (Fig. 3 and Fig. 5) suggest that vivianite authigenesis

560    might also be occurring in the limnic deposits below the sulfidzation front in Black Sea sediments.

561    Assuming that vivianite formation represents the only sink for pore water $HPO_4^{2-}$ results in a good fit between the

562    modeled and measured pore water profile of $HPO_4^{2-}$ below the sulfidization front (Fig. 3). Modeled vivianite

563    formation accounts for up to 70 % of total Fe-associated P directly below the sulfidization front. However, the model

16

564    underestimates the sharp peak in Fe-associated P directly below the sulfidization front, suggesting that modeled

565    vivianite formation likely underestimates the actual contribution of vivianite in these sediments. In the limnic

566    deposits not yet impacted by the downward sulfidization, modeled vivianite accounts for ~ 20 – 30 % of total Fe-

567    associated P. From this, we estimate that vivianite may be responsible for > 20 % of total P burial directly below the

568    sulfidization front and for ~ 10 % of total P burial in the deep limnic deposits at depth.

569    Running the model without Fe-AOM and thus without Fe reduction at depth results in modeled pore water $HPO_4^{2-}$

570    concentrations of up to ~ 350 μM at depth in the sediment (Fig. 8). This suggests that Fe-AOM can promote

571    conditions that allow sequestration of a significant proportion of P as vivianite in the limnic deposits below the

572    sulfidization front. Consistent with earlier findings, Fe-AOM likely only accounts for a small fraction of total $CH_4$

573    oxidation, but may substantially impact the biogeochemical cycling of sedimentary P (Egger et al., 2015a, 2015b;

574    Rooze et al., 2016).

575    The deviation between the modeled and measured profiles of $HPO_4^{2-}$ and Fe-associated P in the upper 300 cm of

576    sediment (Fig. 3 and Fig. 5) could indicate apatite authigenesis (Dijkstra et al., 2014) or the formation of vivianite in

577    microenvironments as previously suggested for sulfidic sediments (Dijkstra et al., 2014; Jilbert and Slomp, 2013).

578    For example, *Deltaproteobacteria*, known to be involved in $SO_4$-AOM, have been shown to accumulate Fe- and P-

579    rich inclusions in their cells (Milucka et al., 2012). They may therefore provide a potential explanation for the

580    occurrence of Fe-associated P in sulfidic sediments (Dijkstra et al., 2014; Jilbert and Slomp, 2013). However, such

581    microenvironments are not captured in our model.

582    In the diagenetic model, vivianite undergoes dissolution if sulfide is present in the pore waters (Table 3). Sulfide-

583    induced vivianite dissolution significantly improved the model fit to the measured $HPO_4^2$ and sulfide data. With the

584    downward migration of dissolved sulfide, modeled vivianite becomes increasingly enriched below the sulfidization

585    front (Fig. 7). Thus, similar to the sulfidization front, a downward diffusive vivianite front may exist in sedimentary

586    systems experiencing downward sulfidzation.

587    In summary, the enhanced downward sulfidization driven by $SO_4$-AOM leads to dissolution of Fe oxide-bound P in

588    the lake deposits. Below the sulfidization front, downward diffusing $HPO_4^{2-}$ is bound again in authigenic vivianite

589    due to high concentrations of dissolved $Fe^{2+}$ at depth in the sediment generated by ongoing Fe oxide reduction. As a

590    result, trends in total P with depth are significantly altered, showing an accumulation in total P below the

591    sulfidization front unrelated to changes in organic matter deposition and enhanced sedimentary P burial during

592    deposition.


593    **5.        Conclusions**

594    In the Black Sea, the shift from a freshwater lake to a marine system and subsequent downward diffusion of marine

595    $SO_4^{2-}$ into the $CH_4$-bearing lake sediments results in a multitude of diagenetic reactions around the SMTZ (Fig. 9).

596    The diagenetic model developed in this study shows that $SO_4$-AOM within the SMTZ significantly enhances the

597    downward diffusive flux of sulfide into the deep limnic deposits, forming a distinct diagenetic sulfidization front

598    around 300 cm depth in the sediment. Our results indicate that without this additional source of dissolved sulfide in

599    the SMTZ, the current sulfidization front would be located around a depth of 150 cm. During the downward

17

sulfidization, Fe oxides, Fe carbonates and vivianite are converted to Fe sulfide phases, leading to an enrichment in solid phase S contents and the release of $HPO_4^{2-}$ to the pore water. Our results further support the hypothesis that part of the downward migrating sulfide is re-oxidized to $SO_4^{2-}$ upon reaction with ferric Fe minerals, fueling a cryptic S cycle and thus stimulating slow rates (~ 1-100 pmol $cm^{-3}$ $d^{-1}$) of $SO_4$-AOM in the $SO_4^{2-}$-depleted limnic deposits below the SMTZ (Holmkvist et al., 2011a, 2011b; Knab et al., 2009; Leloup et al., 2007).

We propose that besides organoclastic Fe oxide reduction and reactivation of less reactive Fe oxides by methanogens, AOM coupled to the reduction of Fe oxides may also be a possible mechanism explaining the high concentrations of $Fe^{2+}$ in the pore water below the sulfidization front. The buildup of dissolved $Fe^{2+}$ at depth creates conditions that allow sequestration of the downward diffusing $HPO_4^{2-}$ as authigenic vivianite, resulting in an accumulation of total P in these sediments.

The diagenetic processes described here reveal that AOM may strongly overprint burial records of Fe, S and P in depositional marine systems subject to changes in organic matter loading or water column salinity such as coastal environments (Egger et al., 2015a; Rooze et al., 2016), deep-sea fan sediments (März et al., 2008; Schulz et al., 1994) and many high-latitude seas (Holmkvist et al., 2014; Treude et al., 2014). Interpreting these diagenetic patterns as primary sedimentary signals may lead to incorrect reconstructions of environmental conditions during sediment deposition.

**References**

Achtnich, C., Bak, F. and Conrad, R.: Competition for electron donors among nitrate reducers, ferric iron reducers, sulfate reducers, and methanogens in anoxic paddy soil, Biol. Fertil. Soils, 19, 65–72, doi:10.1007/BF00336349, 1995.

Alperin, M. J., Reeburgh, W. S. and Whiticar, M. J.: Carbon and hydrogen isotope fractionation resulting from anaerobic methane oxidation, Glob. Biogeochem. Cycl., 2(3), 279–288, doi:10.1029/GB002i003p00279, 1988.

18

634     Amos, R. T., Bekins, B. A., Cozzarelli, I. M., Voytek, M. A., Kirshtein, J. D., Jones, E. J. P. and Blowes, D. W.:

635     Evidence for iron-mediated anaerobic methane oxidation in a crude oil-contaminated aquifer, Geobiology, 10(6),

636     506–17, doi:10.1111/j.1472-4669.2012.00341.x, 2012.

637     Arthur, M. A. and Dean, W. E.: Organic-matter production and evolution of anoxia in the Holocene Black Sea,

638     Paleoceanography, 13(4), 395–411, doi:10.1029/98PA01161, 1998.

639     Beal, E. J., House, C. H. and Orphan, V. J.: Manganese- and iron-dependent marine methane oxidation, Science (80-.

640     )., 325, 184–187, doi:10.1126/science.1169984, 2009.

641     Berg, P., Rysgaard, S. and Thamdrup, B.: Dynamic modeling of early diagenesis and nutrient cycling. A case study

642     in an Arctic marine sediment, Am. J. Sci., 303(10), 905–955, doi:10.2475/ajs.303.10.905, 2003.

643     Berner, R. A.: Iron sulfides in Pleistocene deep Black Sea sediments and their paleo-oceanographic significance, in

644     The Black Sea - Geology, Chemistry and Biology, edited by E. T. Degens and D. A. Ross, pp. 524–531, Plenum

645     Press., 1974.

646     Berner, R. A.: Early Diagenesis: A Theoretical Approach, Princeton University Press., 1980.

647     Bodegom, P. M., Scholten, J. C. M. and Stams, A. J. M.: Direct inhibition of methanogenesis by ferric iron, FEMS

648     Microbiol. Ecol., 49(2), 261–268, doi:10.1016/j.femsec.2004.03.017, 2004.

649     Bond, D. R. and Lovley, D. R.: Reduction of Fe(III) oxide by methanogens in the presence and absence of

650     extracellular quinones, Environ. Microbiol., 4(2), 115–24, doi:10.1046/j.1462-2920.2002.00279.x, 2002.

651     Boudreau, B. P.: The diffusive tortuosity of fine-grained unlithified sediments, Geochim. Cosmochim. Acta, 60(16),

652     3139–3142, doi:10.1016/0016-7037(96)00158-5, 1996.

653     Boudreau, B. P.: Diagenetic models and their implementation. Modelling transport and reactions in aquatic

654     sediments, Springer., 1997.

655     Brass, M. and Röckmann, T.: Continuous-flow isotope ratio mass spectrometry method for carbon and hydrogen

656     isotope measurements on atmospheric methane, Atmos. Meas. Tech., 3(6), 1707–1721, doi:10.5194/amt-3-1707-

657     2010, 2010.

658     Burns, S. J.: Early diagenesis in Amazon fan sediments, in Proceeding of the Ocean Drilling Program, Scientific

659     Results, vol. 155, edited by R. D. Flood, D. J. W. Piper, A. Klaus, and L. C. Peterson, pp. 497–504., 1997.

660     Burton, E. D., Sullivan, L. A., Bush, R. T., Johnston, S. G. and Keene, A. F.: A simple and inexpensive chromium-

661     reducible sulfur method for acid-sulfate soils, Appl. Geochemistry, 23(9), 2759–2766,

662     doi:10.1016/j.apgeochem.2008.07.007, 2008.

663     Capet, A., Beckers, J.-M. and Grégoire, M.: Drivers, mechanisms and long-term variability of seasonal hypoxia on

664     the Black Sea northwestern shelf – is there any recovery after eutrophication?, Biogeosciences, 10, 3943–3962,

665     doi:10.5194/bg-10-3943-2013, 2013.

666     Chanton, J., Chaser, L., Glasser, P. and Siegel, D.: Carbon and hydrogen isotopic effects in microbial methane from

667     terrestrial environments, in Stable isotopes and biosphere-atmosphere interactions, edited by L. Flanagan, pp. 85–

19

668    105, Elsevier-Academic Press., Amsterdam., 2005.

669    Chanton, J. P.: The effect of gas transport on the isotope signature of methane in wetlands, Org. Geochem., 36, 753–

670    768, doi:10.1016/j.orggeochem.2004.10.007, 2005.

671    Claff, S. R., Sullivan, L. A., Burton, E. D. and Bush, R. T.: A sequential extraction procedure for acid sulfate soils:

672    Partitioning of iron, Geoderma, 155(3-4), 224–230, doi:10.1016/j.geoderma.2009.12.002, 2010.

673    Crowe, S. A., Katsev, S., Leslie, K., Sturm, A., Magen, C., Nomosatryo, S., Pack, M. A., Kessler, J. D., Reeburgh,

674    W. S., Roberts, J. A., González, L., Douglas Haffner, G., Mucci, A., Sundby, B. and Fowle, D. A.: The methane

675    cycle in ferruginous Lake Matano, Geobiology, 9(1), 61–78, doi:10.1111/j.1472-4669.2010.00257.x, 2011.

676    Cruz Viggi, C., Rossetti, S., Fazi, S., Paiano, P., Majone, M. and Aulenta, F.: Magnetite particles triggering a faster

677    and more robust syntrophic pathway of methanogenic propionate degradation, Environ. Sci. Technol., 48(13), 7536–

678    7543, doi:10.1021/es5016789, 2014.

679    Degens, E. T. and Ross, D. A.: The Black Sea - geology, chemistry, and biology: American Association of

680    Petroleum Geologists Memoir 20., 1974.

681    Dijkstra, N., Kraal, P., Kuypers, M. M. M., Schnetger, B. and Slomp, C. P.: Are iron-phosphate minerals a sink for

682    phosphorus in anoxic Black Sea sediments?, PLoS One, 9(7), doi:10.1371/journal.pone.0101139, 2014.

683    Eckert, S., Brumsack, H.-J., Severmann, S., Schnetger, B., März, C. and Frollje, H.: Establishment of euxinic

684    conditions in the Holocene Black Sea, Geology, 41(4), 431–434, 2013.

685    Egger, M., Jilbert, T., Behrends, T., Rivard, C. and Slomp, C. P.: Vivianite is a major sink for phosphorus in

686    methanogenic coastal surface sediments, Geochim. Cosmochim. Acta, 169, 217–235, doi:10.1016/j.gca.2015.09.012,

687    2015a.

688    Egger, M., Rasigraf, O., Sapart, C. J., Jilbert, T., Jetten, M. S. M., Röckmann, T., van der Veen, C., Bândă, N.,

689    Kartal, B., Ettwig, K. F. and Slomp, C. P.: Iron-mediated anaerobic oxidation of methane in brackish coastal

690    sediments, Environ. Sci. Technol., 49(1), 277–283, doi:10.1021/es503663z, 2015b.

691    Ettwig, K. F., Butler, M. K., Le Paslier, D., Pelletier, E., Mangenot, S., Kuypers, M. M. M., Schreiber, F., Dutilh, B.

692    E., Zedelius, J., de Beer, D., Gloerich, J., Wessels, H. J. C. T., van Alen, T., Luesken, F., Wu, M. L., van de Pas-

693    Schoonen, K. T., Op den Camp, H. J. M., Janssen-Megens, E. M., Francoijs, K.-J., Stunnenberg, H., Weissenbach, J.,

694    Jetten, M. S. M. and Strous, M.: Nitrite-driven anaerobic methane oxidation by oxygenic bacteria, Nature, 464, 543–

695    548, doi:10.1038/nature08883, 2010.

696    Filippelli, G. M.: Controls on phosphorus concentration and accumulation in oceanic sediments, Mar. Geol., 139(1–

697    4), 231–240, 1997.

698    Froelich, P. N., Klinkhammer, G. P., Bender, M. L., Luedtke, N. A., Heath, G. R., Cullen, D., Dauphin, P.,

699    Hammond, D., Hartman, B. and Maynard, V.: Early oxidation of organic matter in pelagic sediments of the eastern

700    equatorial Atlantic: suboxic diagenesis, Geochim. Cosmochim. Acta, 43(7), 1075–1090, doi:10.1016/0016-

701    7037(79)90095-4, 1979.

702    Grasshoff, K.: A simultaneous multiple channel system for nutrient analysis in seawater with analog and digital data

20

703    record, Contrib. 2338, Woods Hole, 1969.

704    Happell, J. D., Chanton, J. P. and Showers, W. J.: Methane transfer across the water-air interface in stagnant wooded

705    swamps of Florida : Evaluation of mass-transfer coefficients and isotopic fractionation, , 40(2), 290–298, 1995.

706    Henkel, S., Mogollón, J. M., Nöthen, K., Franke, C., Bogus, K., Robin, E., Bahr, A., Blumenberg, M., Pape, T.,

707    Seifert, R., März, C., de Lange, G. J. and Kasten, S.: Diagenetic barium cycling in Black Sea sediments - A case

708    study for anoxic marine environments, Geochim. Cosmochim. Acta, 88, 88–105, doi:10.1016/j.gca.2012.04.021,

709    2012.

710    Hindmarsh, A. C.: ODEPACK, a systematized collection of ODE solvers, in IMACS Transactions on Scientific

711    Computation, Vol. 1, edited by R. S. Stepleman and Others, pp. 55–64, North-Holland, Amsterdam., 1983.

712    Holler, T., Wegener, G., Knittel, K., Boetius, A., Brunner, B., Kuypers, M. M. M. and Widdel, F.: Substantial (13)

713    C/(12) C and D/H fractionation during anaerobic oxidation of methane by marine consortia enriched in vitro,

714    Environ. Microbiol. Rep., 1(5), 370–6, doi:10.1111/j.1758-2229.2009.00074.x, 2009.

715    Holler, T., Wegener, G., Niemann, H., Ferdelman, T. G., Boetius, A., Kristiansen, T. Z., Molina, H., Pandey, A.,

716    Werner, J. K., Juluri, K. R., Xu, Y., Glenn, D., Parang, K. and Snyder, S. H.: Carbon and sulfur back flux during

717    anaerobic microbial oxidation of methane and coupled sulfate reduction, Proc. Natl. Acad. Sci., 109(51), 21170–

718    21170, doi:10.1073/pnas.1218683109, 2012.

719    Holmkvist, L., Ferdelman, T. G. and Jørgensen, B. B.: A cryptic sulfur cycle driven by iron in the methane zone of

720    marine sediment (Aarhus Bay, Denmark), Geochim. Cosmochim. Acta, 75(12), 3581–3599,

721    doi:10.1016/j.gca.2011.03.033, 2011a.

722    Holmkvist, L., Kamyshny, A., Brüchert, V., Ferdelman, T. G. and Jørgensen, B. B.: Sulfidization of lacustrine

723    glacial clay upon Holocene marine transgression (Arkona Basin, Baltic Sea), Geochim. Cosmochim. Acta, 142, 75–

724    94, doi:10.1016/j.gca.2014.07.030, 2014.

725    Holmkvist, L., Kamyshny, A., Vogt, C., Vamvakopoulos, K., Ferdelman, T. G. and Jørgensen, B. B.: Sulfate

726    reduction below the sulfate–methane transition in Black Sea sediments, Deep Sea Res. Part I Oceanogr. Res. Pap.,

727    58(5), 493–504, doi:10.1016/j.dsr.2011.02.009, 2011b.

728    Hsu, T.-W., Jiang, W.-T. and Wang, Y.: Authigenesis of vivianite as influenced by methane-induced sulfidization in

729    cold-seep sediments off southwestern Taiwan, J. Asian Earth Sci., 89, 88–97, doi:10.1016/j.jseaes.2014.03.027,

730    2014.

731    Ingall, E. D., Bustin, R. M. and Van Cappellen, P.: Influence of water column anoxia on the burial and preservation

732    of carbon and phosphorus in marine shales, Geochim. Cosmochim. Acta, 57(2), 303–316, 1993.

733    Jilbert, T. and Slomp, C. P.: Iron and manganese shuttles control the formation of authigenic phosphorus minerals in

734    the euxinic basins of the Baltic Sea, Geochim. Cosmochim. Acta, 107, 155–169, doi:10.1016/j.gca.2013.01.005,

735    2013.

736    Jørgensen, B. B.: A comparison of methods for the quantification of bacterial sulfate reduction in coastal marine

737    sediments. II. Calculations from mathematical models, Geomicrobiol. J., 1, 29–51,

21

738     doi:10.1080/01490457809377721, 1978.

739     Jørgensen, B. B., Böttcher, M. E., Lüschen, H., Neretin, L. N. and Volkov, I. I.: Anaerobic methane oxidation and a
740     deep H2S sink generate isotopically heavy sulfides in Black Sea sediments, Geochim. Cosmochim. Acta, 68(9),
741     2095–2118, doi:10.1016/j.gca.2003.07.017, 2004.

742     Jørgensen, B. B., Weber, A. and Zopfi, J.: Sulfate reduction and anaerobic methane oxidation in Black Sea
743     sediments, Deep Sea Res. Part I Oceanogr. Res. Pap., 48, 2097–2120, doi:10.1016/S0967-0637(01)00007-3, 2001.

744     Kato, S., Hashimoto, K. and Watanabe, K.: Methanogenesis facilitated by electric syntrophy via (semi)conductive
745     iron-oxide minerals, Environ. Microbiol., 14(7), 1646–1654, doi:10.1111/j.1462-2920.2011.02611.x, 2012.

746     Kemp, W. M., Testa, J. M., Conley, D. J., Gilbert, D. and Hagy, J. D.: Temporal responses of coastal hypoxia to
747     nutrient loading and physical controls, Biogeosciences, 6(12), 2985–3008, doi:10.5194/bg-6-2985-2009, 2009.

748     Knab, N. J., Cragg, B. A., Hornibrook, E. R. C., Holmkvist, L., Pancost, R. D., Borowski, C., Parkes, R. J. and
749     Jørgensen, B. B.: Regulation of anaerobic methane oxidation in sediments of the Black Sea, Biogeosciences, (6),
750     1505–1518, doi:10.5194/bg-6-1505-2009, 2009.

751     Knittel, K. and Boetius, A.: Anaerobic oxidation of methane: progress with an unknown process, Annu. Rev.
752     Microbiol., 63, 311–334, doi:10.1146/annurev.micro.61.080706.093130, 2009.

753     Kraal, P. and Slomp, C. P.: Rapid and extensive alteration of phosphorus speciation during oxic storage of wet
754     sediment samples, PLoS One, 9(5), e96859, 2014.

755     Kraal, P., Slomp, C. P., Forster, A. and Kuypers, M. M. M.: Pyrite oxidation during sample storage determines
756     phosphorus fractionation in carbonate-poor anoxic sediments, Geochim. Cosmochim. Acta, 73(11), 3277–3290,
757     doi:10.1016/j.gca.2009.02.026, 2009.

758     Leloup, J., Fossing, H., Kohls, K., Holmkvist, L., Borowski, C. and Jørgensen, B. B.: Sulfate-reducing bacteria in
759     marine sediment (Aarhus Bay, Denmark): abundance and diversity related to geochemical zonation, Environ.
760     Microbiol., 11(5), 1278–1291, doi:10.1111/j.1462-2920.2008.01855.x, 2009.

761     Leloup, J., Loy, A., Knab, N. J., Borowski, C., Wagner, M. and Jørgensen, B. B.: Diversity and abundance of sulfate-
762     reducing microorganisms in the sulfate and methane zones of a marine sediment, Black Sea, Environ. Microbiol.,
763     9(1), 131–142, doi:10.1111/j.1462-2920.2006.01122.x, 2007.

764     Li, H., Chang, J., Liu, P., Fu, L., Ding, D. and Lu, Y.: Direct interspecies electron transfer accelerates syntrophic
765     oxidation of butyrate in paddy soil enrichments, Environ. Microbiol., 17, 1–45, doi:10.1111/1462-2920.12576, 2014.

766     Liu, D., Wang, H., Dong, H., Qiu, X., Dong, X. and Cravotta, C. A.: Mineral transformations associated with
767     goethite reduction by Methanosarcina barkeri, Chem. Geol., 288(1-2), 53–60, doi:10.1016/j.chemgeo.2011.06.013,
768     2011.

769     Lovley, D. R.: Dissimilatory Fe(III) and Mn(IV) reduction, Microbiol. Rev., 55(2), 259–287, 1991.

770     Lovley, D. R. and Phillips, E. J. P.: Competitive mechanisms for inhibition of sulfate reduction and methane
771     production in the zone of ferric iron reduction in sediments, Appl. Environ. Microbiol., 53(11), 1987.

22

772    Lovley, D. R., Phillips, E. J. P. and Lonergan, D. J.: Hydrogen and formate oxidation coupled to dissimilatory
773    reduction of iron or manganese by Alteromonas putrefaciens, Appl. Environ. Microbiol., 55(3), 700–706, 1989.

774    Martens, C. S., Albert, D. B. and Alperin, M. J.: Stable isotope tracing of anaerobic methane oxidation in the gassy
775    sediments of Eckernforde Bay, German Baltic Sea, Am. J. Sci., 299, 589–610, doi:10.2475/ajs.299.7-9.589, 1999.

776    Martens, C. S., Berner, R. A. and Rosenfeld, J. K.: Interstitial water chemistry of anoxic Long Island Sound
777    sediments. 2. Nutrient regeneration and phosphate removal, Limnol. Oceanogr., 23(4), 605–617, 1978.

778    März, C., Hoffmann, J., Bleil, U., de Lange, G. J. and Kasten, S.: Diagenetic changes of magnetic and geochemical
779    signals by anaerobic methane oxidation in sediments of the Zambezi deep-sea fan (SW Indian Ocean), Mar. Geol.,
780    255(3-4), 118–130, doi:10.1016/j.margeo.2008.05.013, 2008.

781    Meysman, F. J. R., Boudreau, B. P. and Middelburg, J. J.: Modeling reactive transport in sediments subject to
782    bioturbation and compaction, Geochim. Cosmochim. Acta, 69(14), 3601–3617, doi:10.1016/j.gca.2005.01.004,
783    2005.

784    Milucka, J., Ferdelman, T. G., Polerecky, L., Franzke, D., Wegener, G., Schmid, M., Lieberwirth, I., Wagner, M.,
785    Widdel, F. and Kuypers, M. M. M.: Zero-valent sulphur is a key intermediate in marine methane oxidation, Nature,
786    491(7425), 541–6, doi:10.1038/nature11656, 2012.

787    Mogollón, J. M., Dale, A. W., Jensen, J. B., Schlüter, M. and Regnier, P.: A method for the calculation of anaerobic
788    oxidation of methane rates across regional scales: An example from the Belt Seas and The Sound (North Sea-Baltic
789    Sea transition), Geo-Marine Lett., 33(4), 299–310, doi:10.1007/s00367-013-0329-z, 2013.

790    Moodley, L., Middelburg, J. J., Herman, P. M. J., Soetaert, K. and de Lange, G. J.: Oxygenation and organic-matter
791    preservation in marine sediments: Direct experimental evidence from ancient organic carbon–rich deposits, Geology,
792    33(11), 889, doi:10.1130/G21731.1, 2005.

793    Mort, H. P., Slomp, C. P., Gustafsson, B. G. and Andersen, T. J.: Phosphorus recycling and burial in Baltic Sea
794    sediments with contrasting redox conditions, Geochim. Cosmochim. Acta, 74(4), 1350–1362,
795    doi:10.1016/j.gca.2009.11.016, 2010.

796    Murphy, J. and Riley, J. P.: A modified single solution method for the determination of phosphate in natural waters,
797    Anal. Chim. Acta, 27, 31–36, doi:10.1016/S0003-2670(00)88444-5, 1962.

798    Neretin, L. N., Böttcher, M. E., Jørgensen, B. B., Volkov, I. I., Lüschen, H. and Hilgenfeldt, K.: Pyritization
799    processes and greigite formation in the advancing sulfidization front in the Upper Pleistocene sediments of the Black
800    Sea, Geochim. Cosmochim. Acta, 68(9), 2081–2093, doi:10.1016/S0016-7037(00)00450-2, 2004.

801    Petzoldt, L. R.: Automatic selection of methods for solving stiff and nonstiff systems of ordinary differential
802    equations, SIAM J. Sci. Stat. Comput., 4, 136–148, doi:10.1137/0904010, 1983.

803    Poulton, S. and Canfield, D.: Development of a sequential extraction procedure for iron: implications for iron
804    partitioning in continentally derived particulates, Chem. Geol., 214(3-4), 209–221,
805    doi:10.1016/j.chemgeo.2004.09.003, 2005.

806    Qu, D., Ratering, S. and Schnell, S.: Microbial reduction of weakly crystalline iron (III) oxides and suppression of

23

807    methanogenesis in paddy soil, Bull. Environ. Contam. Toxicol., 72(6), 1172–1181, doi:10.1007/s00128-004-0367-3,
808    2004.

809    Raghoebarsing, A. A., Pol, A., van de Pas-Schoonen, K. T., Smolders, A. J. P., Ettwig, K. F., Rijpstra, W. I. C.,
810    Schouten, S., Damsté, J. S. S., Op den Camp, H. J. M., Jetten, M. S. M. and Strous, M.: A microbial consortium
811    couples anaerobic methane oxidation to denitrification, Nature, 440(7086), 918–921, doi:10.1038/nature04617, 2006.

812    Raiswell, R. and Canfield, D. E.: The iron biogeochemical cycle past and present, Geochemical Perspect., 1(1),
813    doi:10.7185/geochempersp.1.1, 2012.

814    Rayleigh, J. W. S.: Theoretical considerations respecting the separation of gases by diffusion and similar processes,
815    Philos. Mag., (42), 493–499, 1896.

816    Reeburgh, W.: Oceanic methane biogeochemistry, Am. Chem. Soc., 107(2), 486–513, doi:10.1021/cr050362v, 2007.

817    Reed, D. C., Slomp, C. P. and Gustafsson, B. G.: Sedimentary phosphorus dynamics and the evolution of bottom-
818    water hypoxia: A coupled benthic-pelagic model of a coastal system, Limnol. Oceanogr., 56(3), 1075–1092,
819    doi:10.4319/lo.2011.56.3.1075, 2011a.

820    Reed, D. C., Slomp, C. P. and de Lange, G. J.: A quantitative reconstruction of organic matter and nutrient
821    diagenesis in Mediterranean Sea sediments over the Holocene, Geochim. Cosmochim. Acta, 75(19), 5540–5558,
822    doi:10.1016/j.gca.2011.07.002, 2011b.

823    Regnier, P., Dale, A. W., Arndt, S., LaRowe, D. E., Mogollón, J. and Van Cappellen, P.: Quantitative analysis of
824    anaerobic oxidation of methane (AOM) in marine sediments: A modeling perspective, Earth-Science Rev., 106(1-2),
825    105–130, doi:10.1016/j.earscirev.2011.01.002, 2011.

826    Reiche, M., Torburg, G. and Küsel, K.: Competition of Fe(III) reduction and methanogenesis in an acidic fen, FEMS
827    Microbiol. Ecol., 65(1), 88–101, doi:10.1111/j.1574-6941.2008.00523.x, 2008.

828    Rickard, D. and Luther, G. W.: Kinetics of pyrite formation by the H2S oxidation of iron (II) monosulfide in aqueous
829    solutions between 25 and 125°C: The mechanism, Geochim. Cosmochim. Acta, 61(1), 135–147, doi:10.1016/S0016-
830    7037(96)00322-5, 1997.

831    Riedinger, N., Formolo, M. J., Lyons, T. W., Henkel, S., Beck, A. and Kasten, S.: An inorganic geochemical
832    argument for coupled anaerobic oxidation of methane and iron reduction in marine sediments, Geobiology,
833    doi:10.1111/gbi.12077, 2014.

834    Rooze, J., Egger, M., Tsandev, I. and Slomp, C. P.: Iron-dependent anaerobic oxidation of methane in coastal surface
835    sediments: potential controls and impact, Limnol. Oceanogr., doi:10.1002/lno.10275, 2016.

836    Ruttenberg, K. C.: Development of a sequential extraction method for different forms of phosphorus in marine
837    sediments, Limnol. Oceanogr., 37(7), 1460–1482, 1992.

838    Ruttenberg, K. C. and Berner, R. A.: Authigenic apatite formation and burial in sediments from non-upwelling,
839    continental margin environments, Geochim. Cosmochim. Acta, 57(5), 991–1007, doi:10.1016/0016-7037(93)90035-
840    U, 1993.

24

841 Van Santvoort, P. J. M., De Lange, G. J., Thomson, J., Colley, S., Meysman, F. J. R. and Slomp, C. P.: Oxidation
842 and origin of organic matter in surficial Eastern Mediterranean hemipelagic sediments, Aquat. Geochemistry, 8(3),
843 153–175, doi:10.1023/A:1024271706896, 2002.

844 Sapart, C. J., van der Veen, C., Vigano, I., Brass, M., van de Wal, R. S. W., Bock, M., Fischer, H., Sowers, T.,
845 Buizert, C., Sperlich, P., Blunier, T., Behrens, M., Schmitt, J., Seth, B. and Röckmann, T.: Simultaneous stable
846 isotope analysis of methane and nitrous oxide on ice core samples, Atmos. Meas. Tech., 4(12), 2607–2618,
847 doi:10.5194/amt-4-2607-2011, 2011.

848 Scheller, S., Yu, H., Chadwick, G. L., McGlynn, S. E. and Orphan, V. J.: Artificial electron acceptors decouple
849 archaeal methane oxidation from sulfate reduction, Science (80-. )., 351(6274), 703–707,
850 doi:10.1126/science.aad7154, 2016.

851 Schulz, H. D., Dahmke, A., Schinzel, U., Wallmann, K. and Zabel, M.: Early diagenetic processes, fluxes, and
852 reaction rates in sediments of the South Atlantic, Geochim. Cosmochim. Acta, 58(9), 2041–2060, doi:10.1016/0016-
853 7037(94)90284-4, 1994.

854 Segarra, K. E. A., Comerford, C., Slaughter, J. and Joye, S. B.: Impact of electron acceptor availability on the
855 anaerobic oxidation of methane in coastal freshwater and brackish wetland sediments, Geochim. Cosmochim. Acta,
856 115, 15–30, doi:10.1016/j.gca.2013.03.029, 2013.

857 Seifert, R., Nauhaus, K., Blumenberg, M., Krüger, M. and Michaelis, W.: Methane dynamics in a microbial
858 community of the Black Sea traced by stable carbon isotopes in vitro, Org. Geochem., 37(10), 1411–1419,
859 doi:10.1016/j.orggeochem.2006.03.007, 2006.

860 Sivan, O., Adler, M., Pearson, A., Gelman, F., Bar-Or, I., John, S. G. and Eckert, W.: Geochemical evidence for
861 iron-mediated anaerobic oxidation of methane, Limnol. Oceanogr., 56(4), 1536–1544,
862 doi:10.4319/lo.2011.56.4.1536, 2011.

863 Sivan, O., Antler, G., Turchyn, A. V., Marlow, J. J. and Orphan, V. J.: Iron oxides stimulate sulfate-driven anaerobic
864 methane oxidation in seeps, Proc. Natl. Acad. Sci., 1–9, doi:10.1073/pnas.1412269111, 2014.

865 Sivan, O., Shusta, S. and Valentine, D. L.: Methanogens rapidly transition from methane production to iron
866 reduction, Geobiology, doi:10.1111/gbi.12172, 2016.

867 Slomp, Van der Gaast, S. J. and Van Raaphorst, W.: Phosphorus binding by poorly crystalline iron oxides in North
868 Sea sediments, Mar. Chem., 52(1), 55–73, doi:10.1016/0304-4203(95)00078-X, 1996a.

869 Slomp, C. P., Epping, E. H. G., Helder, W. and Raaphorst, W. Van: A key role for iron-bound phosphorus in
870 authigenic apatite formation in North Atlantic continental platform sediments, J. Mar. Res., 54(6), 1179–1205,
871 doi:10.1357/0022240963213745, 1996b.

872 Slomp, C. P., Mort, H. P., Jilbert, T., Reed, D. C., Gustafsson, B. G. and Wolthers, M.: Coupled dynamics of iron
873 and phosphorus in sediments of an oligotrophic coastal basin and the impact of anaerobic oxidation of methane.,
874 PLoS One, 8(4), e62386, doi:10.1371/journal.pone.0062386, 2013.

875 Soetaert, K., Herman, P. M. J. and Middelburg, J. J.: A model of early diagenetic processes from the shelf to abyssal

25

876 depths, Geochim. Cosmochim. Acta, 60(6), 1019–1040, doi:10.1016/0016-7037(96)00013-0, 1996.

877 Soetaert, K. and Meysman, F.: Reactive transport in aquatic ecosystems: Rapid model prototyping in the open source
878 software R, Environ. Model. Softw., 32, 49–60, doi:10.1016/j.envsoft.2011.08.011, 2012.

879 Soetaert, K., Petzoldt, T. and Meysman, F. J. R.: marelac: Tools for Aquatic Sciences. R Package Version 2.1.3,
880 2010.

881 Soulet, G., Delaygue, G., Vallet-Coulomb, C., Böttcher, M. E., Sonzogni, C., Lericolais, G. and Bard, E.: Glacial
882 hydrologic conditions in the Black Sea reconstructed using geochemical pore water profiles, Earth Planet. Sci. Lett.,
883 296(1-2), 57–66, doi:10.1016/j.epsl.2010.04.045, 2010.

884 Soulet, G., Ménot, G., Lericolais, G. and Bard, E.: A revised calendar age for the last reconnection of the Black Sea
885 to the global ocean, Quat. Sci. Rev., 30(9-10), 1019–1026, doi:10.1016/j.quascirev.2011.03.001, 2011.

886 Stoll, M. H. C., Bakker, K., Nobbe, G. H. and Haese, R. R.: Continous-Flow Analysis of Dissolved Inorganic Carbon
887 Content in Seawater, Anal. Chem., 73(17), 4111–4116, doi:10.1021/ac010303r, 2001.

888 Strickland, J. D. and Parsons, T. R.: A Practical Handbook of Seawater Analysis, Bulletin 1., Fisheries Research
889 Board of Canada, Ottawa, Canada., 1972.

890 Suess, E.: Mineral phases formed in anoxic sediments by microbial decomposition of organic matter, Geochim.
891 Cosmochim. Acta, 43, 339–352, doi:10.1016/0016-7037(79)90199-6, 1979.

892 Thamdrup, B., Roselló-Mora, R. and Amann, R.: Microbial manganese and sulfate reduction in Black Sea shelf
893 sediments, Appl. Environ. Microbiol., 66(2251), 2288–2297, doi:10.1128/AEM.66.7.2888-2897.2000, 2000.

894 Treude, T., Krause, S., Maltby, J., Dale, A. W., Coffin, R. and Hamdan, L. J.: Sulfate reduction and methane
895 oxidation activity below the sulfate-methane transition zone in Alaskan Beaufort Sea continental margin sediments:
896 Implications for deep sulfur cycling, Geochim. Cosmochim. Acta, 144, 217–237, doi:10.1016/j.gca.2014.08.018,
897 2014.

898 Vargas, M., Kashefi, K., Blunt-Harris, E. L. and Lovley, D. R.: Microbial evidence for Fe(III) reduction on early
899 Earth, Nature, 395, 65–67, doi:10.1038/25720, 1998.

900 Wang, Y. and Van Cappellen, P.: A multicomponent reactive transport model of early diagenesis : Application to
901 redox cycling in coastal marine sediments, Geochim. Cosmochim. Acta, 60(16), 2993–3014, doi:10.1016/0016-
902 7037(96)00140-8, 1996.

903 Wankel, S. D., Adams, M. M., Johnston, D. T., Hansel, C. M., Joye, S. B. and Girguis, P. R.: Anaerobic methane
904 oxidation in metalliferous hydrothermal sediments: influence on carbon flux and decoupling from sulfate reduction,
905 Environ. Microbiol., 14(10), 2726–40, doi:10.1111/j.1462-2920.2012.02825.x, 2012.

906 Whiticar, M. J.: Carbon and hydrogen isotope systematics of bacterial formation and oxidation of methane, Chem.
907 Geol., 161(1-3), 291–314, doi:10.1016/S0009-2541(99)00092-3, 1999.

908 Yoshinaga, M. Y., Holler, T., Goldhammer, T., Wegener, G., Pohlman, J. W., Brunner, B., Kuypers, M. M. M.,
909 Hinrichs, K. and Elvert, M.: Carbon isotope equilibration during sulphate-limited anaerobic oxidation of methane,

910 Nat. Geosci., 7, 190–194, doi:10.1038/NGEO2069, 2014.

911 Zhou, S., Xu, J., Yang, G. and Zhuang, L.: Methanogenesis affected by the co-occurrence of iron(III) oxides and
912 humic substances, FEMS Microbiol. Ecol., 88(1), 107–120, doi:10.1111/1574-6941.12274, 2014.

913 Zhuang, L., Xu, J., Tang, J. and Zhou, S.: Effect of ferrihydrite biomineralization on methanogenesis in an anaerobic
914 incubation from paddy soil, J. Geophys. Res. Biogeosciences, (120), 876–886, doi:10.1002/2014JG002893, 2015.

915

916

27

**Tables**

918 **Table 1. Overview of the sequential P, Fe and S fractionation methods used in this study.**

| Step and code | Extractant, extraction time | Target phase |
|---|---|---|
| **P fractionation (modified from Ruttenberg (1992); done for site 4 (MC & GC) and site 5 (MC & GC))** | | |
| **1 $P_{exch}$** | 1 M $MgCl_2$, pH 8, 0.5 h | Exchangeable P |
| **2[a] $P_{Fe}$** | 25 g $L^{-1}$ Na dithionite, pH 7.5, 8 h | Fe-associated P |
| **3[a] $P_{authi\ Ca-P}$** | Na acetate buffer, pH 4, 6 h | P in authigenic and biogenic Ca-P minerals and $CaCO_3$ |
| **4 $P_{detr}$** | 1 M HCl, 24 h | Detrital P |
| **5 $P_{org}$** | Ashing at 550 °C (2h), then 1 M HCl, 24 h | Organic P |
| **Fe fractionation (after Poulton and Canfield (2005); done for site 4 (MC & GC) and site 5 (MC))** | | |
| **1 $Fe_{carb}$** | 1 M Na acetate, pH 4.5, 24 h | Carbonate-associated Fe |
| **2 $Fe_{ox1}$** | 1 M hydroxylamine-HCl, 24 h | Amorphous Fe oxides (ferrihydrite) |
| **3 $Fe_{ox2}$** | 50 g $L^{-1}$ Na dithionite, pH 4.8, 2 h | Crystalline Fe oxides (goethite, hematite) |
| **4 $Fe_{mag}$** | 0.2 M ammonium oxalate/ 0.17 M oxalic acid, 2 h | Recalcitrant Fe oxides (mostly magnetite) |
| **Fe fractionation (modified from Claff et al. (2010); done for site 4 (MC & GC) and site 5 (MC))** | | |
| **1 $Fe(II)_{HCl}$** | 1 M HCl, 4 h | Labile Fe (carbonates, poorly ordered sulfides) |
| **2 $Fe(III)_{HCl}$** | 1 M HCl, 4 h | Labile Fe (easily reducible oxides) |
| **3 $Fe(III)_{CDB}$** | 50 g $L^{-1}$ Na dithionite, pH 4.8, 4 h | Crystalline Fe oxides |
| **4 $Fe_{pyrite}$** | Concentrated $HNO_3$, 2 h | Pyrite ($FeS_2$) |
| **S fractionation (after Burton et al. (2008); done for site 4 (MC) and site 5 (MC & GC))** | | |
| **1 AVS** | 6 M HCl, 24 h | S in Fe monosulfides (FeS) |
| **2 CRS** | Acidic chromous chloride solution, 48 h | S in pyrite ($FeS_2$) |

919 [a] These steps were followed by a wash step with 1 M $MgCl_2$, which was added to the corresponding step. MC = multicore and GC

920 = gravity core.

921

922    **Table 2. Chemical species included in the diagenetic model.**

| Species | Notation | Type |
|---|---|---|
| Organic matter[a] | $OM^{\alpha,\beta,\gamma}$ | Solid |
| Iron oxides[a] | $Fe(OH)_3^{\alpha,\beta,\gamma}$ | Solid |
| Iron monosulfide | $FeS$ | Solid |
| Pyrite | $FeS_2$ | Solid |
| Siderite | $FeCO_3$ | Solid |
| Elemental sulfur | $S_0$ | Solid |
| Iron oxide-bound phosphorus | $Fe_{ox}P$ | Solid |
| Vivianite | $Fe_3(PO_4)_2$ | Solid |
| Organic phosphorus | $P_{org}$ | Solid |
| Authigenic (Ca) phosphorus | $CaP$ | Solid |
| Detrital phosphorus | $DetrP$ | Solid |
| Chloride | $Cl^-$ | Solute |
| Oxygen | $O_2$ | Solute |
| Sulfate | $SO_4^{2-}$ | Solute |
| Iron | $Fe^{2+}$ | Solute |
| Hydrogen sulfide[b] | $\sum H_2S$ | Solute |
| Methane | $CH_4$ | Solute |
| Ammonium[b] | $\sum NH_4^+$ | Solute |
| Nitrate | $NO_3^-$ | Solute |
| Phosphate | $\sum HPO_4^{2-}$ | Solute |
| Dissolved inorganic carbon | $DIC$ | Solute |

923    [a] There are three types of species: reactive (α), less reactive (β) and refractory (γ)

924    [b] $\sum$ denotes that all species of an acid are included

925

29

**Table 3. Reaction pathways and stoichiometries implemented in the diagenetic model.**

**Primary redox reactions***

| | |
|---|---|
| $OM^{\propto,\beta} + aO_2 \rightarrow aCO_2 + bNH_4^+ + cH_3PO_4 + aH_2O$ | R1 |
| $OM^{\propto,\beta} + \frac{4a}{5}NO_3^- + \frac{4a}{5}H^+ \rightarrow aCO_2 + bNH_4^+ + cH_3PO_4 + \frac{2a}{5}N_2 + \frac{7a}{5}H_2O$ | R2 |
| $OM^{\propto,\beta} + 4aFe(OH)_3^\propto + 4a\chi^\propto Fe_{ox}P + 12aH^+ \rightarrow aCO_2 + bNH_4^+ + (c + 4a\chi^\propto)H_3PO_4 + 4aFe^{2+} + 13aH_2O$ | R3 |
| $OM^{\propto,\beta} + \frac{a}{2}SO_4^{2-} + aH^+ \rightarrow aCO_2 + bNH_4^+ + cH_3PO_4 + \frac{a}{2}H_2S + aH_2O$ | R4 |
| $OM^{\propto,\beta} \rightarrow \frac{a}{2}CO_2 + bNH_4^+ + cH_3PO_4 + \frac{a}{2}CH_4$ | R5 |
| $CO_2 + 4H_2 \rightarrow CH_4 + 2H_2O$ | R6 |

**Secondary redox and other reaction equations**[†]

| | |
|---|---|
| $2O_2 + NH_4^+ + 2HCO_3^- \rightarrow NO_3^- + 2CO_2 + 3H_2O$ | R7 |
| $O_2 + 4Fe^{2+} + 8HCO_3^- + 2H_2O + 4\chi^\propto H_2PO_4^- \rightarrow 4Fe(OH)_3^\propto + 4\chi^\propto Fe_{ox}P + 8CO_2$ | R8 |
| $2O_2 + FeS \rightarrow SO_4^{2-} + Fe^{2+}$ | R9 |
| $7O_2 + 2FeS_2 + 2H_2O \rightarrow 4SO_4^{2-} + 2Fe^{2+} + 4H^+$ | R10 |
| $2O_2 + H_2S + 2HCO_3^- \rightarrow SO_4^{2-} + 2CO_2 + 2H_2O$ | R11 |
| $2O_2 + CH_4 \rightarrow CO_2 + 2H_2O$ | R12 |
| $2Fe(OH)_3^\propto + 2\chi^\propto Fe_{ox}P + H_2S + 4CO_2 \rightarrow 2Fe^{2+} + 2\chi^\propto H_2PO_4^- + S_0 + 4HCO_3^- + 2H_2O$ | R13 |
| $2Fe(OH)_3^\beta + 2\chi^\beta Fe_{ox}P + H_2S + 4CO_2 \rightarrow 2Fe^{2+} + 2\chi^\beta H_2PO_4^- + S_0 + 4HCO_3^- + 2H_2O$ | R14 |
| $Fe^{2+} + H_2S \rightarrow FeS + 2H^+$ | R15 |
| $FeS + H_2S \rightarrow FeS_2 + H_2$ | R16 |
| $4S_0 + 4H_2O \rightarrow 3H_2S + SO_4^{2-} + 2H^+$ | R17 |
| $FeS + S_0 \rightarrow FeS_2$ | R18 |
| $SO_4^{2-} + CH_4 + CO_2 \rightarrow 2HCO_3^- + H_2S$ | R19 |
| $CH_4 + 8Fe(OH)_3^{\propto,\beta} + 8\chi^{\propto,\beta}Fe_{ox}P + 15H^+ \rightarrow HCO_3^- + 8Fe^{2+} + 8\chi^{\propto,\beta}H_2PO_4^- + 21H_2O$ | R20 |
| $Fe(OH)_3^\propto + (\chi^\propto - \chi^\beta)Fe_{ox}P \rightarrow Fe(OH)_3^\beta + (\chi^\propto - \chi^\beta)H_2PO_4^-$ | R21 |
| $Fe(OH)_3^\beta + (\chi^\beta - \chi^\gamma)Fe_{ox}P \rightarrow Fe(OH)_3^\gamma + (\chi^\beta - \chi^\gamma)H_2PO_4^-$ | R22 |
| $3Fe^{2+} + 2HPO_4^{2-} \rightarrow Fe_3(PO_4)_2 + 2H^+$ | R23 |
| $Fe^{2+} + CO_3^{2-} \rightarrow FeCO_3$ | R24 |
| $FeCO_3 + H_2S \rightarrow FeS + HCO_3^- + H^+$ | R25 |
| $Fe_3(PO_4)_2 + 3H_2S \rightarrow 3FeS + 2HPO_4^{2-} + 4H^+$ | R26 |

* Organic matter (OM) is of the form $(CH_2O)_a(NH_4^+)_b(H_3PO_4)_c$, with 'a'=1, 'b' = 1/16 and 'c' = 1/106. Under anoxic bottom water conditions, 'c' reduces to 0.25 to account for the preferential regeneration of P (e.g. Ingall et al. (1993)). † $\chi^{\propto,\beta,\gamma}$refers to the P:Fe ratio of $Fe(OH)_3^{\propto,\beta,\gamma}$ (see Supplementary Table S1). *R6* = CH₄ production from DIC (i.e. CO₂)*; R7* = nitrification; *R8* = Fe(OH)₃ formation; *R9* = FeS oxidation; *R10* = FeS₂ oxidation; *R11* = H₂S oxidation; *R12* = aerobic CH₄ oxidation; *R13* and *R14* = Fe(OH)₃ reduction by H₂S; *R15*= FeS formation; *R16* = pyrite formation (H₂S pathway); *R17* = S₀ disproportionation; *R18* = pyrite formation (polysulfide pathway); *R19* = SO₄-AOM; *R20* = Fe-AOM; *R21* = conversion (i.e. crystallization) from α to β phase; *R22* = crystallization from β to γ phase; *R23* = vivianite formation; *R24* = siderite precipitation; *R25* = conversion from siderite to FeS; *R26* = vivianite dissolution by dissolved sulfide

937   **Table 4. Reaction equations implemented in the model.**

| Primary redox reaction equations | |
|---|---|

$$R_1 = k_{\propto,\beta} OM^{\propto,\beta} \left( \frac{[O_2]}{K_{O_2}+[O_2]} \right)$$ (E1)

$$R_2 = k_{\propto,\beta} OM^{\propto,\beta} \left( \frac{[NO_3^-]}{K_{NO_3^-}+[NO_3^-]} \right) \left( \frac{K_{O_2}}{K_{O_2}+[O_2]} \right)$$ (E2)

$$R_3 = k_{\propto,\beta} OM^{\propto,\beta} \left( \frac{[Fe(OH)_3^\alpha]}{K_{Fe(OH)_3^\alpha}+[Fe(OH)_3^\alpha]} \right) \left( \frac{K_{NO_3^-}}{K_{NO_3^-}+[NO_3^-]} \right) \left( \frac{K_{O_2}}{K_{O_2}+[O_2]} \right)$$ (E3)

$$R_4 = \Psi k_{\propto,\beta} OM^{\propto,\beta} \left( \frac{[SO_4^{2-}]}{K_{SO_4^{2-}}+[SO_4^{2-}]} \right) \left( \frac{K_{Fe(OH)_3^\alpha}}{K_{Fe(OH)_3^\alpha}+[Fe(OH)_3^\alpha]} \right) \left( \frac{K_{NO_3^-}}{K_{NO_3^-}+[NO_3^-]} \right) \left( \frac{K_{O_2}}{K_{O_2}+[O_2]} \right)$$ (E4)

$$R_5 = \Psi k_{\propto,\beta} OM^{\propto,\beta} \left( \frac{K_{SO_4^{2-}}}{K_{SO_4^{2-}}+[SO_4^{2-}]} \right) \left( \frac{K_{Fe(OH)_3^\alpha}}{K_{Fe(OH)_3^\alpha}+[Fe(OH)_3^\alpha]} \right) \left( \frac{K_{NO_3^-}}{K_{NO_3^-}+[NO_3^-]} \right) \left( \frac{K_{O_2}}{K_{O_2}+[O_2]} \right)$$ (E5)

$$R_6 = k_1 DIC \left( \frac{K_{SO_4^{2-}}}{K_{SO_4^{2-}}+[SO_4^{2-}]} \right) \left( \frac{K_{Fe(OH)_3^\alpha}}{K_{Fe(OH)_3^\alpha}+[Fe(OH)_3^\alpha]} \right) \left( \frac{K_{NO_3^-}}{K_{NO_3^-}+[NO_3^-]} \right) \left( \frac{K_{O_2}}{K_{O_2}+[O_2]} \right)$$ (E6)

| Secondary redox and other reaction equations | |
|---|---|

$$R_7 = k_2 [O_2][NH_4^+]$$ (E7)

$$R_8 = k_3 [O_2][Fe^{2+}]$$ (E8)

$$R_9 = k_4 [O_2][FeS]$$ (E9)

$$R_{10} = k_5 [O_2][FeS_2]$$ (E10)

$$R_{11} = k_6 [O_2][\sum H_2 S]$$ (E11)

$$R_{12} = k_7 [O_2][CH_4]$$ (E12)

$$R_{13} = k_8 [Fe(OH)_3^\propto][\sum H_2 S]$$ (E13)

$$R_{14} = k_9 [Fe(OH)_3^\beta][\sum H_2 S]$$ (E14)

$$R_{15} = k_{10} [Fe^{2+}][\sum H_2 S]$$ (E15)

$$R_{16} = k_{11} [FeS][\sum H_2 S]$$ (E16)

$$R_{17} = k_{12} [S_0]$$ (E17)

$$R_{18} = k_{13} [FeS][S_0]$$ (E18)

$$R_{19} = k_{14} [SO_4^{2-}][CH_4]$$ (E19)

$$R_{20} = k_{15} [Fe(OH)_3^{\propto,\beta}][CH_4]$$ (E20)

$$R_{21} = k_{16} [Fe(OH)_3^\propto]$$ (E21)

$$R_{22} = k_{17} [Fe(OH)_3^\beta]$$ (E22)

$$R_{23} = k_{18} [Fe^{2+}][HPO_4^{2-}]$$ (E23)

$$R_{24} = k_{19} [Fe^{2+}][DIC]$$ (E24)

$$R_{25} = k_{20} [FeCO_3][\sum H_2 S]$$ (E25)

$$R_{26} = k_{21} [Fe_3(PO_4)_2][\sum H_2 S]$$ (E26)

938

939

940 **Table 5. Reaction parameters used in the diagenetic model.**

| Parameter | Symbol | Value | Units | Values given in literature |
|---|---|---|---|---|
| Decay constant for $OM^{\alpha}$ | $k_{\alpha}$ | 0.05 | $yr^{-1}$ | 0.05-1.62[a,b] |
| Decay constant for $OM^{\beta}$ | $k_{\beta}$ | 0.0086 | $yr^{-1}$ | 0.0086[b] |
| Limiting concentration of $O_2$ | $K_{O2}$ | 0.02 | mM | 0.001-0.03[c] |
| Limiting concentration of $NO_3^-$ | $K_{NO3^-}$ | 0.004 | mM | 0.004-0.08[c] |
| Limiting concentration of $Fe(OH)_3$ | $K_{Fe(OH)3}$ | 65 | $\mu mol\ g^{-1}$ | 65-100[c] |
| Limiting concentration of $SO_4^{2-}$ | $K_{SO42^-}$ | 1.6 | mM | 1.6[c] |
| Attenuation factor for $SO_4^{2-}$ and methanogenesis | $\Psi$ | 0.0042 | - | 0.00157-0.075[b,d] |
| Rate constant for reaction *E6* | $k_1$ | 0.0011 | $yr^{-1}$ | |
| Rate constant for reaction *E7* | $k_2$ | 10'000 | $mM^{-1}\ yr^{-1}$ | 5'000-39'000[c,d] |
| Rate constant for reaction *E8* | $k_3$ | 140'000 | $mM^{-1}\ yr^{-1}$ | 140'000[c] |
| Rate constant for reaction *E9* | $k_4$ | 300 | $mM^{-1}\ yr^{-1}$ | 300[c] |
| Rate constant for reaction *E10* | $k_5$ | 1 | $mM^{-1}\ yr^{-1}$ | 1[c] |
| Rate constant for reaction *E11* | $k_6$ | 160 | $mM^{-1}\ yr^{-1}$ | $\geq$ 160[c] |
| Rate constant for reaction *E12* | $k_7$ | 10'000'000 | $mM^{-1}\ yr^{-1}$ | 10'000'000[c] |
| Rate constant for reaction *E13* | $k_8$ | 9.5 | $mM^{-1}\ yr^{-1}$ | $\leq$ 100[c] |
| Rate constant for reaction *E14* | $k_9$ | 0.95 | $mM^{-1}\ yr^{-1}$ | Model constrained |
| Rate constant for reaction *E15* | $k_{10}$ | 150 | $mM^{-1}\ yr^{-1}$ | 100-14'800[b, d] |
| Rate constant for reaction *E16* | $k_{11}$ | 0.0003 | $mM^{-1}\ yr^{-1}$ | 3.15[e] |
| Rate constant for reaction *E17* | $k_{12}$ | 3 | $yr^{-1}$ | 3[f] |
| Rate constant for reaction *E18* | $k_{13}$ | 1 | $mM^{-1}\ yr^{-1}$ | 7[f] |
| Rate constant for reaction *E19* | $k_{14}$ | 0.14 | $mM^{-1}\ yr^{-1}$ | 10[c] |
| Rate constant for reaction *E20* | $k_{15}$ | 0.00000016 | $mM^{-1}\ yr^{-1}$ | 0.0074[g] |
| Rate constant for reaction *E21* | $k_{16}$ | 0.6 | $yr^{-1}$ | 0.6[f] |
| Rate constant for reaction *E22* | $k_{17}$ | 0.000013 | $yr^{-1}$ | Model constrained |
| Rate constant for reaction *E23* | $k_{18}$ | 0.052 | $mM^{-1}\ yr^{-1}$ | Model constrained |
| Rate constant for reaction *E24* | $k_{19}$ | 0.0027 | $mM^{-1}\ yr^{-1}$ | Model constrained |
| Rate constant for reaction *E25* | $k_{20}$ | 0.0008 | $mM^{-1}\ yr^{-1}$ | Model constrained |
| Rate constant for reaction *E26* | $k_{21}$ | 0.0008 | $mM^{-1}\ yr^{-1}$ | Model constrained |

941 [a] Moodley et al. (2005); [b] Reed et al. (2011a); [c] Wang and Van Cappellen (1996); [d] Reed et al. (2011b); [e] Rickard and Luther
942 (1997); [f] Berg et al. (2003); [g] Rooze et al. (2016)

943

944

945

946    **Table 6. Depth-integrated rates of key processes for selected depth intervals in μmol m$^{-2}$ d$^{-1}$.**

| Process | 0 – 90 cm[a] | 90 - 300 cm[b] | 300 – 800 cm[c] | 0 – 800 cm |
|---|---|---|---|---|
| Organoclastic SO$_4^{2-}$ reduction[d] | 68.9 | 5.3 | 0.003 | 74.2 |
| CH$_4$ production[e,f] | 10.21 | 37.7 | 91.8 | 139.8 |
| SO$_4$ - AOM | 9.4 | 151.6 | 1.2 | 162.2 |
| Fe – AOM[e] | 0 | 0 | 1.2 | 1.2 |
| S$_0$ disproportionation | 0 | 0 | 0.9 | 0.9 |

947    [a] Marine deposits ; [b] limnic sediments around the SMTZ with dissolved sulfide; [c] non-sulfidic limnic deposits; [d] per mol of SO$_4^{2-}$; [e]

948    per mol of CH$_4$; [f] sum of CH$_4$ production from organic matter and from DIC (i.e. CO$_2$)

949

950

951

952    **Figures**
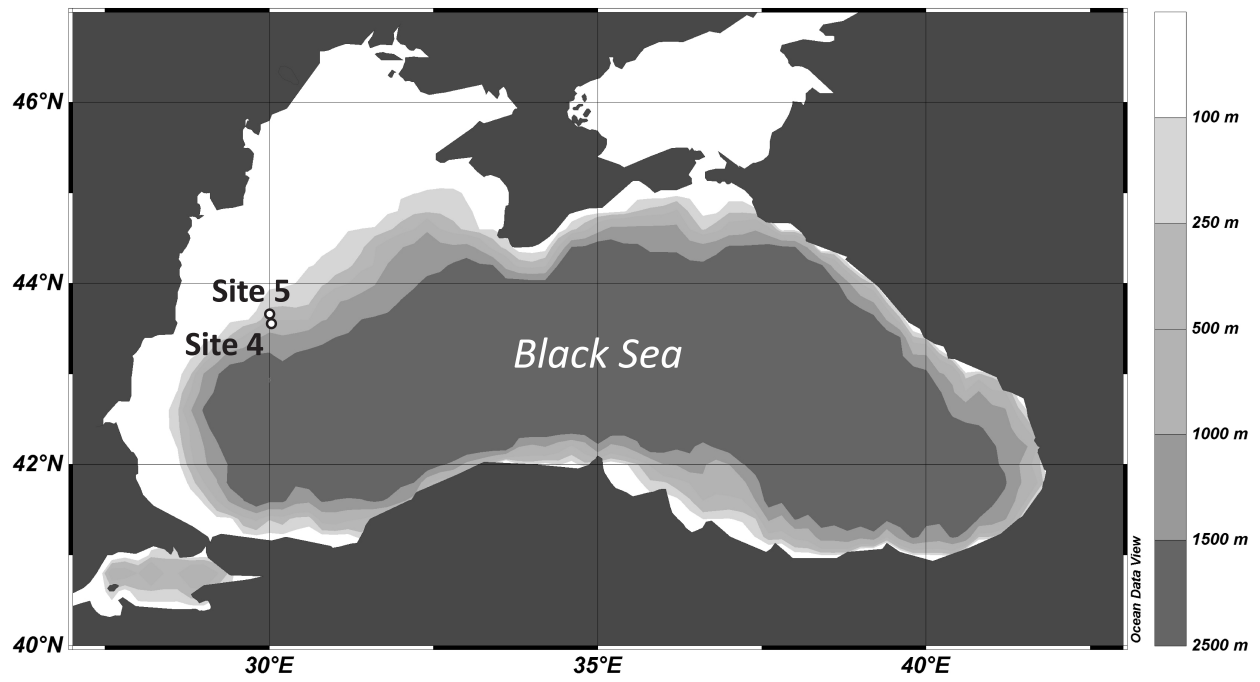


953

954    Figure 1. Map showing the locations of site 4 (43°40.6' N, 30°7.5' E; 377 mbss) and site 5 (43°42.6' N, 30°6.1' E; 178 mbss),
955    sampled in June 2013.

956

957

34
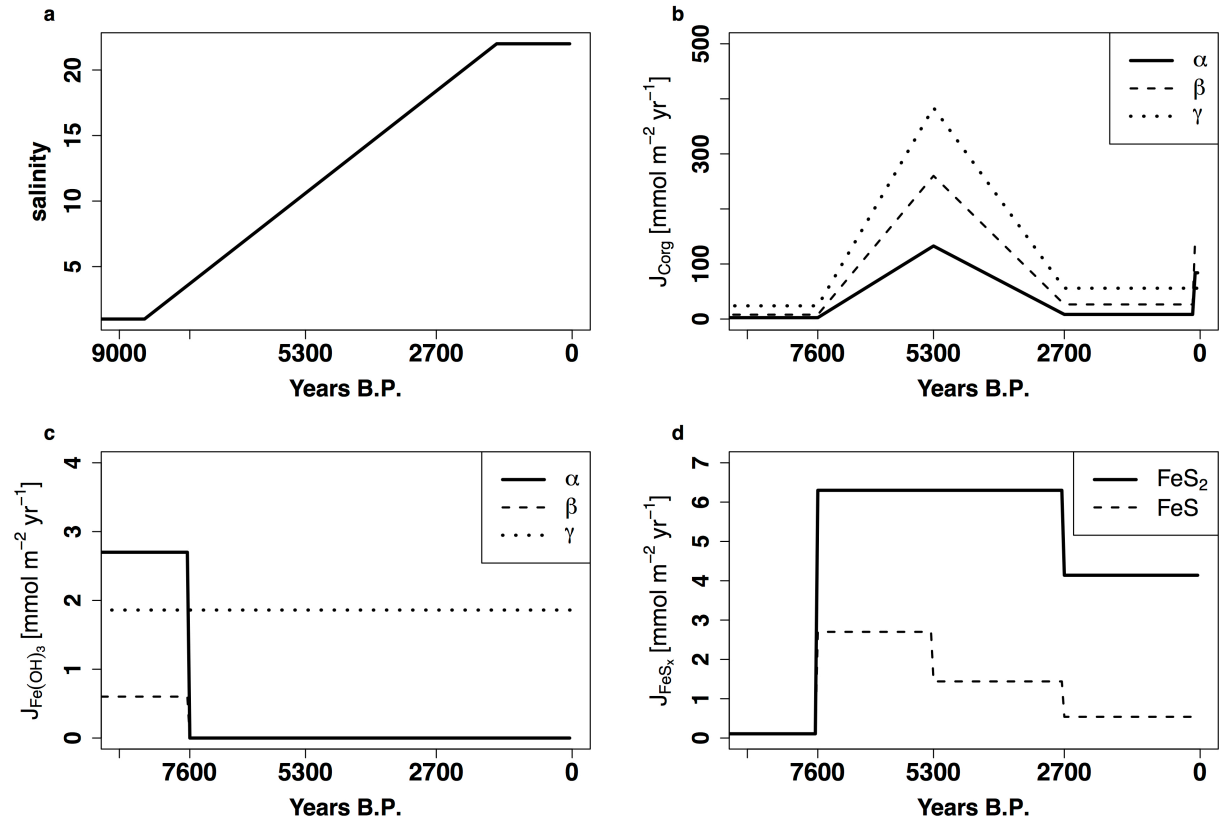
958

959　Figure 2. Transient evolution of salinity with a linear increase from 1 to 22 between 8500 and 1500 years B.P. (a), fluxes of
960　organic matter ($J_{C_{Org}}$; b), Fe oxides ($J_{Fe(OH)_3}$; c) and Fe sulfides ($J_{FeS_x}$; d) as implemented in the diagenetic model (site 4).

961

962
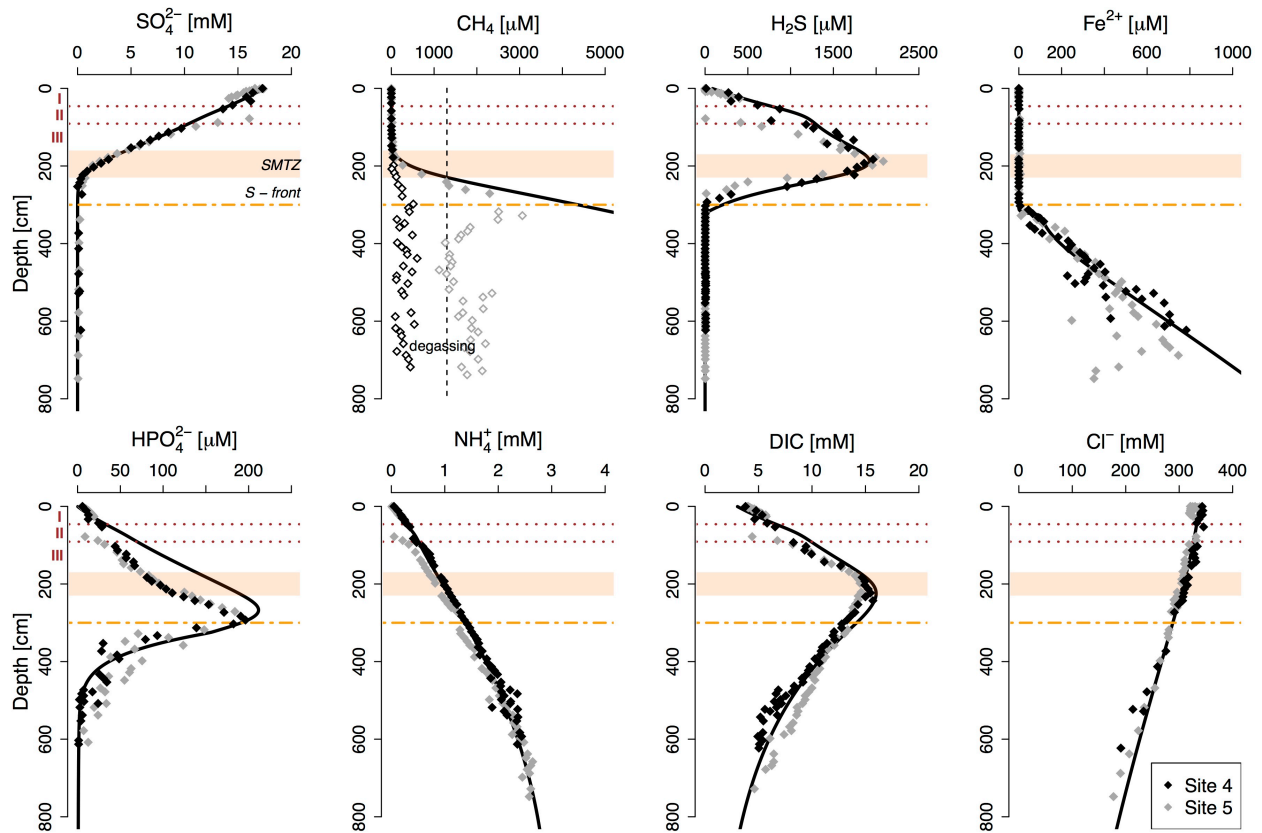
Figure 3. Pore water profiles of key components for site 4 (black diamonds) and site 5 (gray diamonds) and corresponding modeled profiles as calculated with the diagenetic model (black lines). Red dotted lines and roman numbers indicate the transitions between the lithological Unit I (modern coccolith ooze), Unit II (marine sapropel) and Unit III (limnic deposits). The orange bar represents the sulfate-methane transition zone (SMTZ) and the orange dashed line shows the current position of the downward migrating sulfidization front (S-front). The dashed vertical line indicates the $CH_4$ saturation concentration at atmospheric pressure (Mogollón et al., 2013). The open diamonds indicate $CH_4$ concentrations that are likely underestimated due to outgassing of $CH_4$ during coring.

970

971

36

972
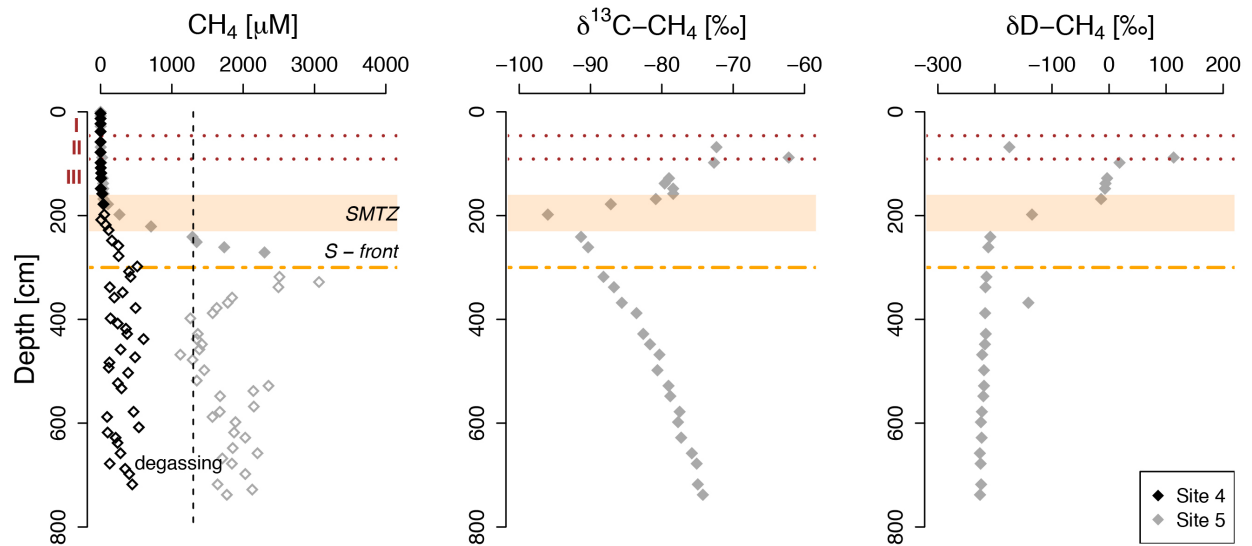
**Figure 4.** Pore water profiles of CH$_4$ for site 4 (black diamonds) and 5 (gray diamonds) and corresponding isotopic composition of dissolved CH$_4$ (available for site 5 only). δ$^{13}$C-CH$_4$ values are given in ‰ vs. VPDB (Vienna Pee Dee Belemnite) and δD-CH$_4$ values are given in ‰ vs. V-SMOW (Vienna Standard Mean Ocean Water). Red dotted lines and roman numbers indicate the transitions between the lithological Unit I (modern coccolith ooze), Unit II (marine sapropel) and Unit III (limnic deposits). The orange bar represents the sulfate-methane transition zone (SMTZ) and the orange dashed line shows the current position of the downward migrating sulfidization front (S-front). The dashed vertical line indicates the CH$_4$ saturation concentration at atmospheric pressure (Mogollón et al., 2013). The open diamonds indicate CH$_4$ concentrations that are likely underestimated due to outgassing of CH$_4$ during coring.

981

37
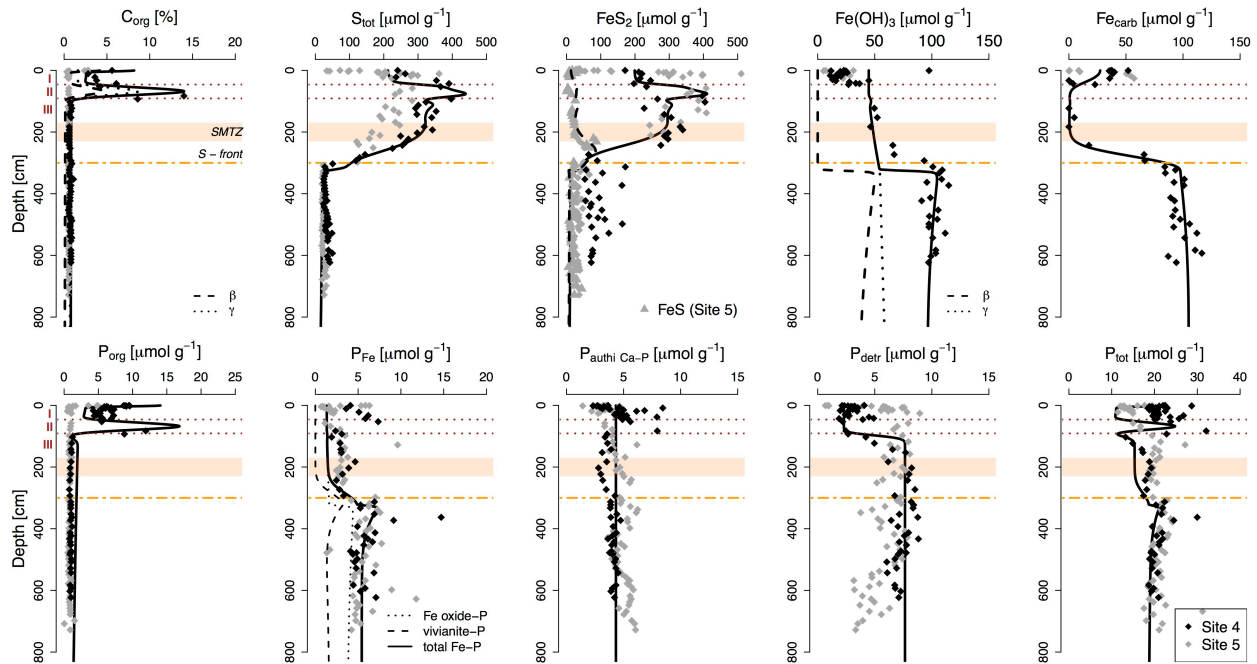
**Figure 5. Solid phase sediment profiles for site 4 (black diamonds) and 5 (gray diamonds). Fe oxides represent the sum of amorphous, crystalline and recalcitrant oxides, i.e. $Fe_{ox1}$, $Fe_{Ox2}$ and $Fe_{mag}$ (Table 1, Supplementary Fig. S4). $Fe_{carb}$ was corrected for apparent AVS dissolution during the Na acetate extraction step (the uncorrected $Fe_{carb}$ data is given in Supplementary Fig. S4). Black lines represent profiles derived from the diagenetic model. Red dotted lines and roman numbers indicate the transitions between the lithological Unit I (modern coccolith ooze), Unit II (marine sapropel) and Unit III (limnic deposits). The orange bar represents the sulfate-methane transition zone (SMTZ) and the orange dashed line shows the current position of the downward migrating sulfidization front (S-front).**

38
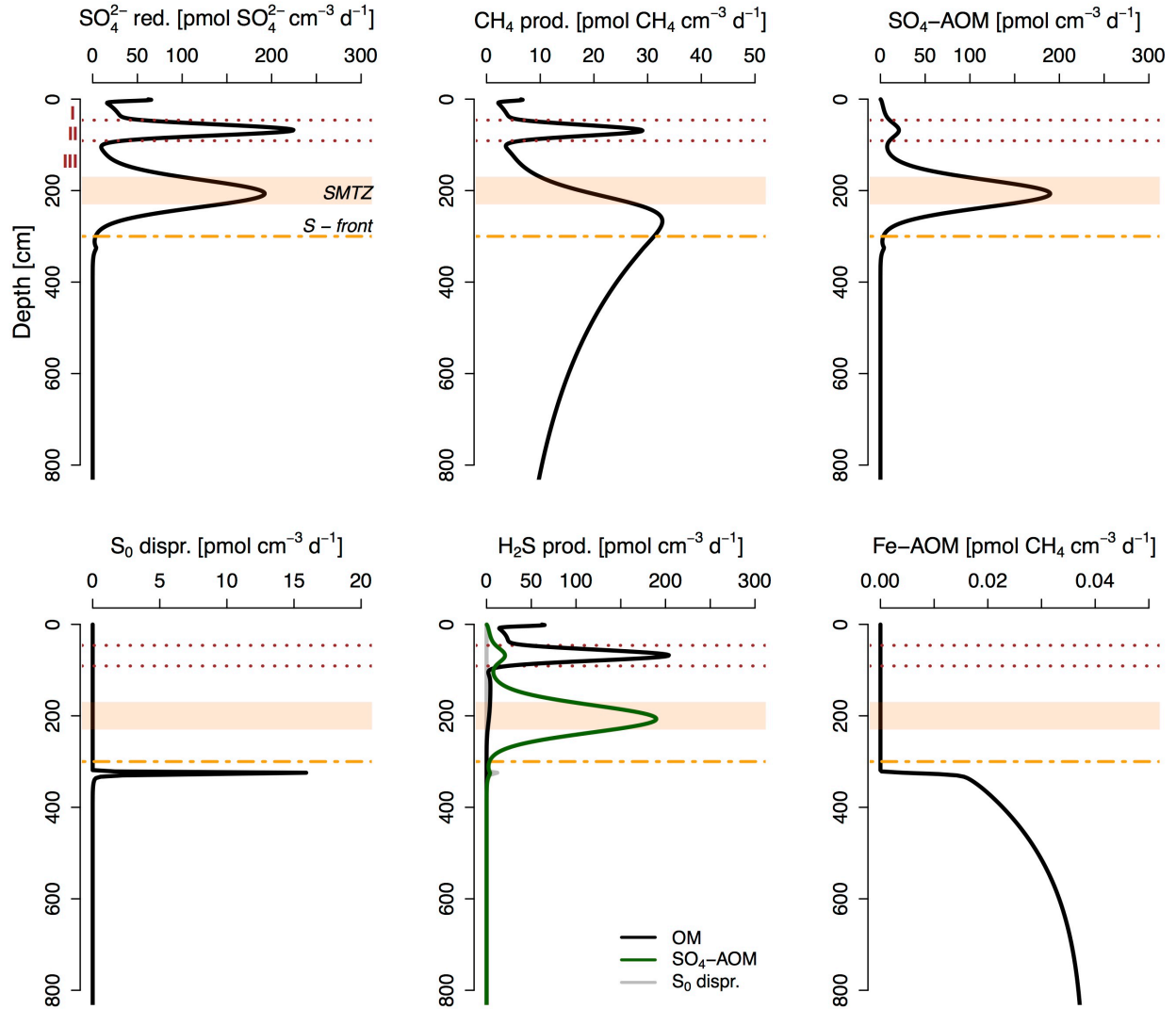
**Figure 6. Modeled rates of total $SO_4^{2-}$ reduction, total $CH_4$ production, $SO_4$-AOM, $S_0$ disproportionation, sulfide production and Fe-AOM. Red dotted lines and roman numbers indicate the transitions between the lithological Unit I (modern coccolith ooze), Unit II (marine sapropel) and Unit III (limnic deposits). The orange bar represents the sulfate-methane transition zone (SMTZ) and the orange dashed line shows the current position of the downward migrating sulfidization front (S-front).**
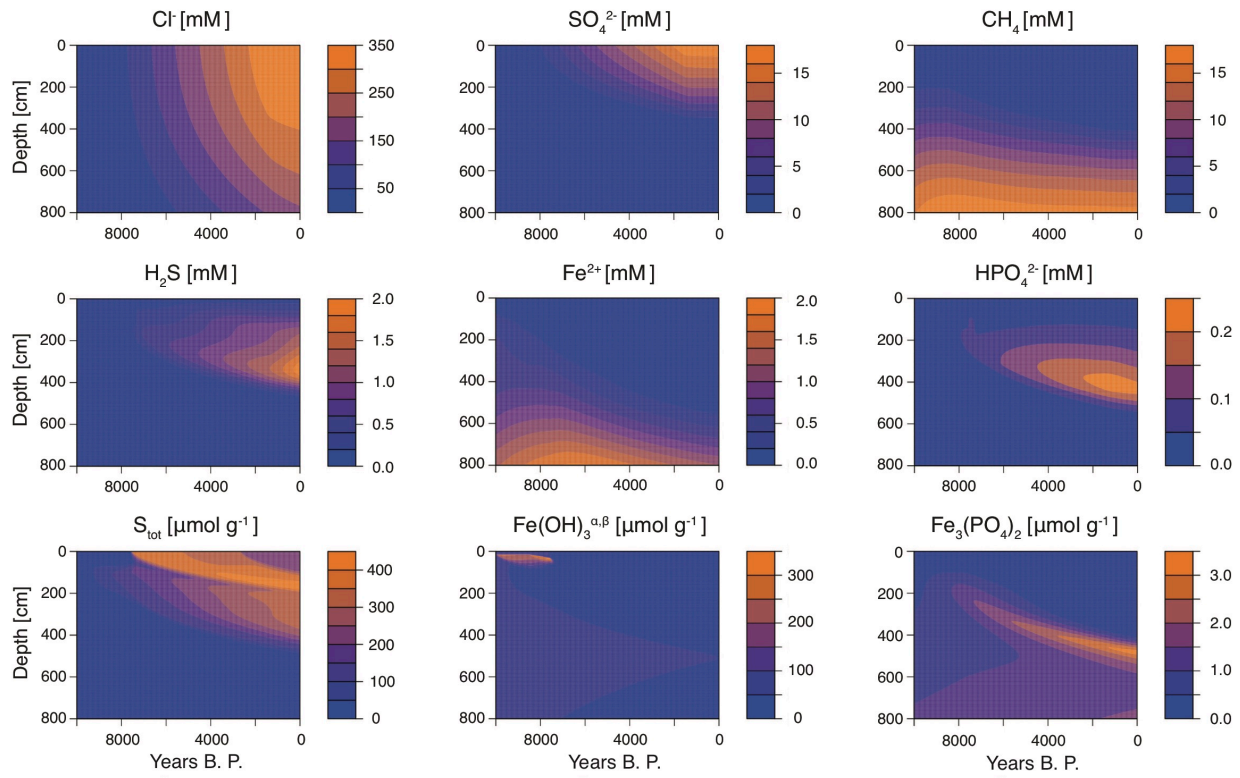
998

999 **Figure 7. Transient evolution of selected pore water and sediment profiles with depth as calculated for site 4 using the**

1000 **diagenetic model.**

1001

40

1002
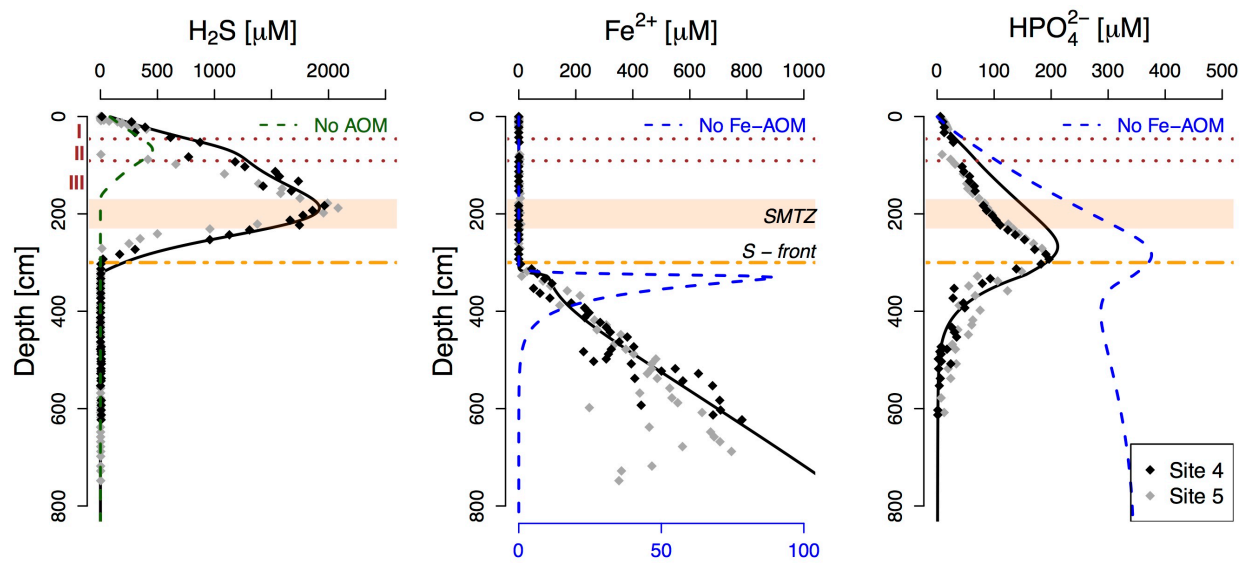


1003

1004 **Figure 8. Pore water profiles of dissolved sulfide, $Fe^{2+}$ and $HPO_4^{2-}$. The green dashed line represents the modeled sulfide**

1005 **profile without $SO_4$-AOM, indicating that the latter significantly enhances the downward sulfidization. Blue dashed lines**

1006 **denote the modeled $Fe^{2+}$ and $HPO_4^{2-}$ profiles without ongoing Fe oxide reduction in the limnic deposits (i.e. no Fe-AOM).**

1007 **Note that concentrations of $Fe^{2+}$ were multiplied 10 times in the model simulation without Fe oxide reduction to better**

1008 **visualize the potential release of $Fe^{2+}$ through a cryptic S cycle (corresponding x axis at bottom). Red dotted lines and**

1009 **roman numbers indicate the transitions between the lithological Unit I (modern coccolith ooze), Unit II (marine sapropel)**

1010 **and Unit III (limnic deposits). The orange bar represents the sulfate-methane transition zone (SMTZ) and the orange**

1011 **dashed line shows the current position of the downward migrating sulfidization front (S-front).**

1012
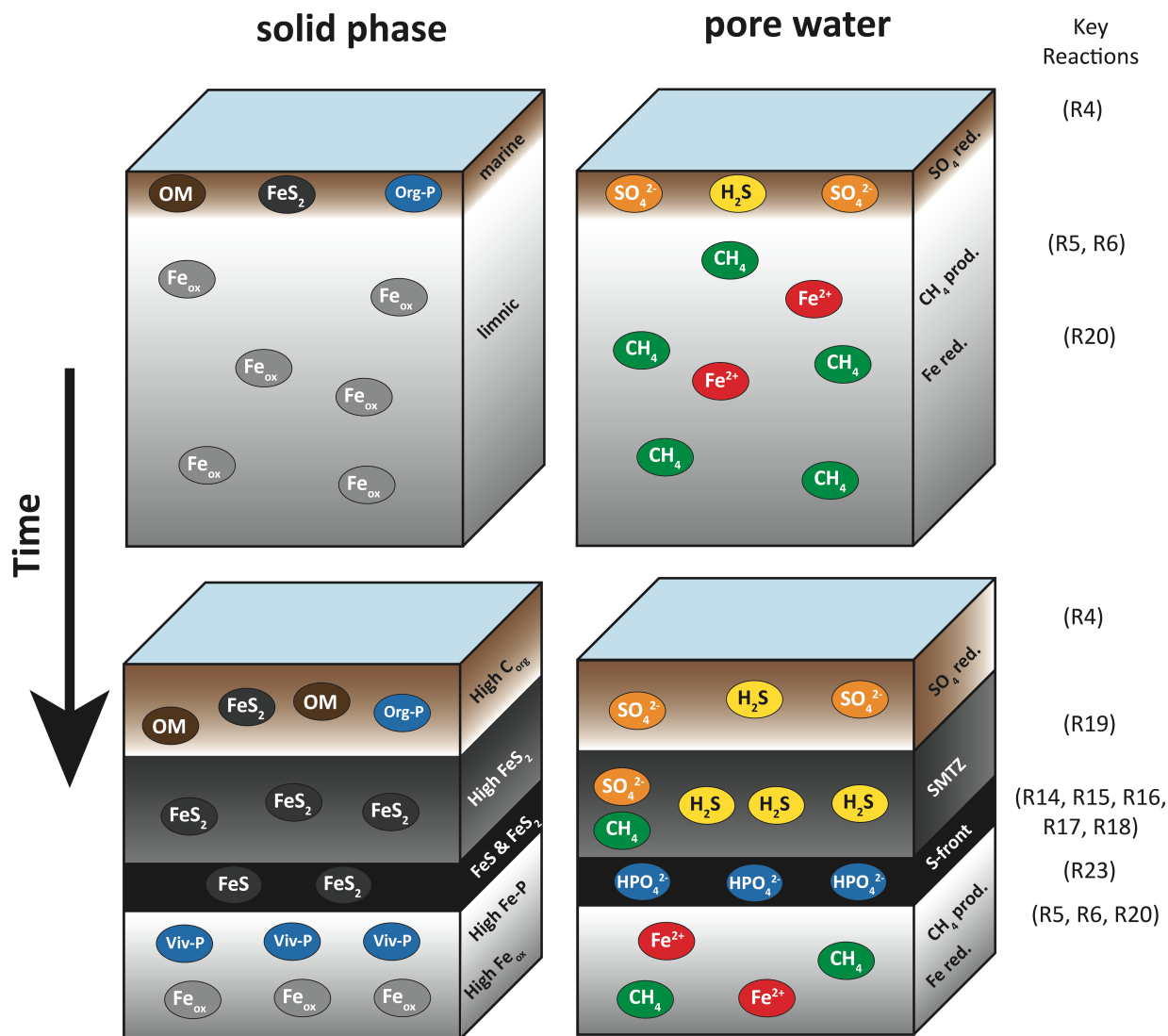
1013

1014    **Figure 9. Schematic of the main diagenetic processes discussed in this study and their imprint on the geochemical solid**

1015    **phase (left) and pore water profiles (right). Accumulation of marine sediments with time and the subsequent downward**

1016    **diffusion of $SO_4^{2-}$ into the $CH_4$-bearing limnic sediment stimulate $SO_4$-AOM around the sulfate-methane transition zone**

1017    **(SMTZ), thus enhancing the downward sulfidization of the Fe oxide-rich lake deposits. Below the sulfidization front (S-**

1018    **front), $HPO_4^{2-}$ released during reductive dissolution of Fe oxides is bound again in vivianite, leading to an enrichment in**

1019    **sedimentary P in these sediments. Numbers on the right indicate the key reactions occurring in the corresponding**

1020    **sediment layers as described in Table 3. Note that in this study, Fe-AOM (R20) was assumed as the main source of pore**

1021    **water $Fe^{2+}$ below the S-front to further test the potential impact of Fe-AOM on pore water $CH_4$. However, based on the**

1022    **geochemical data, we cannot exclude a potential role for organoclastic Fe reduction (R3) and/or reactivation of less**

1023    **reactive Fe oxides by methanogens.**